TABLE 1
Log P and Brain Uptake After Intravenous Administration of ^{18}F-Labeled Compounds in Mice

Compound	Log P	Brain uptake (%ID/g) 2 min after injection	30 min after injection	60 min after injection	Brain uptake ratio (2 min/60 min)
^{18}F-THK-523	2.40	2.72	1.47	1.46	1.86
^{18}F-THK-5105	3.03	9.20	3.61	1.00	9.20
^{18}F-THK-5116	1.57	3.36	0.75	0.57	5.89
^{18}F-THK-5117	2.32	6.06	0.59	0.26	23.1
^{18}F-FDDNP	3.71	6.23	2.02	2.14	2.91

Aβ1–42 and K18ΔK280-tau were prepared as described previously (*15*). Briefly, synthetic Aβ1–42 (200 μM) and K18Δ280K-tau (20 μM) solutions in phosphate-buffered saline (PBS) were incubated at 37° C with agitation for 3–4 d. We additionally prepared AD brain homogenates for binding assay, because the structural conformation of synthetic protein fibrils does not fully correlate with the structure of native protein deposits in the human brain. Human brain tissue was isolated from a mesial temporal frozen sample of an AD patient and homogenized in PBS. Brain tissue homogenate aliquots were taken and frozen at −80°C until used. Insoluble Aβ and tau levels were determined using a human β-amyloid enzyme-linked immunosorbent assay (ELISA) kit (Wako) and a human tau ELISA kit (Life Technologies Japan Ltd.), respectively. Next, brain homogenates and the solutions of synthetic Aβ1–42 or K18Δ280K-tau fibrils were incubated with increasing concentrations of ^{18}F-THK-5105 (0.1–250 nM). To account for nonspecific binding of ^{18}F-THK-5105, the reactions were performed in triplicate in the presence of 2 μM unlabeled THK-5105. The binding reactions were incubated for 1 h at room temperature in assay buffer (Dulbecco PBS; 0.1% bovine serum albumin). Bound radioactive compounds were separated from free radioactive compounds by filtration under reduced pressure (MultiScreen HTS Vacuum Manifold; Millipore). Filters were washed three times with assay buffer, and the radioactivity contained within the filters was counted in a γ-counter (AccuFLEX γ7000, Aloka, Tokyo, Japan). Binding data were analyzed using curve-fitting software that calculates the K_d and B_{max} (K_d is dissociation constant and B_{max} is maximum number of binding sites, respectively) using nonlinear regression (GraphPad Prism; GraphPad Software).

For inhibition studies, the assay buffer containing each compound (0.1–1,000 nM), ^{18}F-THK-5105 (1.76 nM, ~37 kBq), K18Δ280K-tau (200 nM), and 0.1% bovine serum albumin was incubated at room temperature for 1 h. Nonspecific binding was determined in the presence of 10 μM THK-5105. The mixture was filtered through Multiscreen HTS 96-well filtration plates, followed by washing three times with PBS (0.1% bovine serum albumin), and the filters containing bound ^{18}F ligand were counted in a γ-counter. The percentage of bound radioligand at each concentration was measured in triplicate and then plotted against the inhibitor concentration. Half-maximal inhibitory concentration values were determined from the displacement curves using the GraphPad Prism software. Inhibition constant (K_i) values were calculated from the half-maximal inhibitory concentration values using the Cheng–Prusoff equation (*28*).

TABLE 2
K_d and B_{max} Values of ^{18}F-THK-5105 for Synthetic Tau and $Aβ_{1–42}$ Fibrils

Protein	K_{d1}	B_{max1}	K_{d2}	B_{max2}
Tau	1.45	6.89	7.40	20.05
$Aβ_{1–42}$	35.9	61.6		

K_d are in nM and Bmax are in pmol ^{18}F-THK-5105/nmol fibrils.

Tissue Staining

Experiments were performed under the regulations of the ethics committee of Tohoku University School of Medicine. Paraffin-embedded hippocampal brain sections from an autopsy-confirmed AD case (78-y-old woman) were used for tissue staining with THK-5105. Brain sections were obtained from Fukushimura Hospital. After deparaffinization, autofluorescence quenching was performed as previously described (*29*). Quenched tissue sections were immersed for 10 min in a 100-μM THK-5105 solution containing 50% ethanol. Sections were then dipped briefly into water, rinsed in PBS, coverslipped with FluorSave Reagent (Calbiochem), and examined using an Eclipse microscope (Nikon) equipped with a blue-violet filter (excitation, 400–440 nm; dichroic mirror, 455 nm; barrier filter, 470 nm). Sections stained with THK-5105 were subsequently immunostained with the AT8 anti-tau antibody (diluted 1:20; Innogenetics). After incubation at 4°C in the primary antibody for 16 h, sections were processed by the avidin-biotin method using a Pathostain ABC-POD(M) Kit (Wako) and diaminobenzidine as a chromogen. Sections were additionally stained using a modified Gallyas–Braak method (pretreatment with 0.3% potassium permanganate for 10 min, followed by 0.1% oxalic acid for 3 min) (*30*).

Autoradiography of Human Brain Sections

For the autoradiographic study, 8-μm-thick paraffin-embedded brain sections from a healthy control (62-y-old man) and 2 AD patients (69-y-old man and 92-y-old woman) were used. After deparaffinization, sections were incubated for 10 min at room temperature with radiolabeled compounds (0.5 MBq/mL) and washed briefly with water and 50% ethanol. After being dried, the labeled sections were exposed overnight to a BAS-III imaging plate (Fuji Film). The autoradiographic images were obtained using a BAS-5000 phosphoimaging instrument (Fuji Film). The neighboring sections were stained

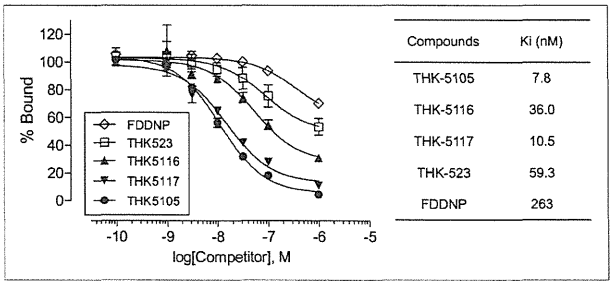

FIGURE 3. Competitive inhibition of ^{18}F-THK-5105 binding by 2-arylquinolines and FDDNP to tau protein fibrils. K_i values for inhibition of ^{18}F-THK-5105 binding to tau are shown.

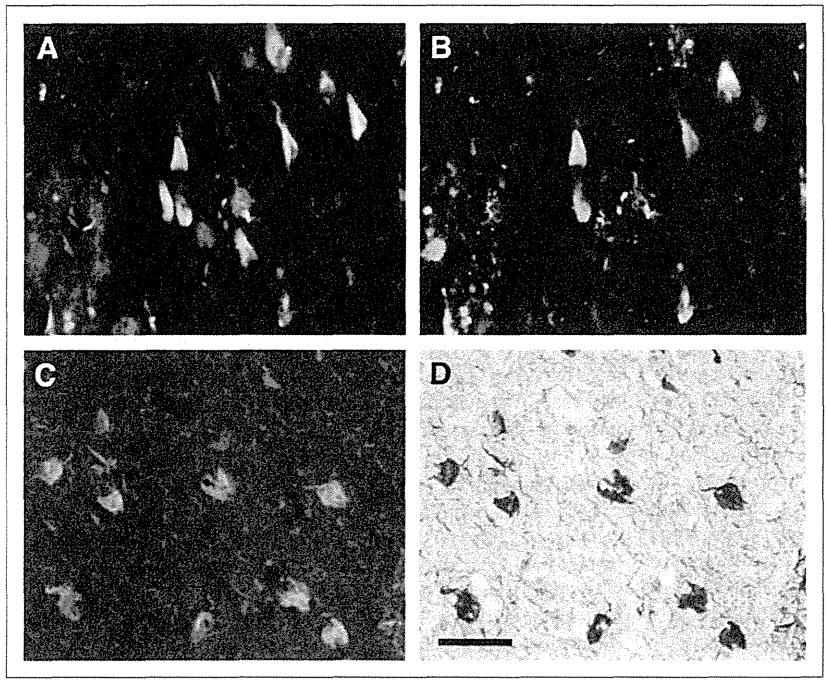

FIGURE 4. Neuropathologic staining of brain sections from AD patients. Neurofibrillary tangles and neuropil threads were clearly stained with THK-5105 (A and C). These stainings were consistent with tau immunostaining (B) and Gallyas–Braak staining (D) in same sections. Bar = 50 μm.

using a modified Gallyas–Braak method or immunostained using the AT8 anti-tau monoclonal antibody (diluted 1:20; Innogenetics), the 4G8 Aβ antibody (diluted 1:100; Signet), or the 6F/3D Aβ antibody (diluted 1:50; Dako). For correlational analysis of the autoradiographic and immunohistochemical images, 36 circular regions of interest (the area of each region of interest was ~7 mm^2) were placed on the gray matter of the hippocampus, parahippocampal gyrus, fusiform gyrus, temporal gyri (superior, middle, and inferior), insula, pre- and postcentral gyri, superior frontal gyrus, paracentral lobule, and cingulate gyrus. The percentage area of positive signals in each region of interest was calculated using ImageJ software (National Institutes of Health). A correlational analysis between percentage areas of tracer binding and positive immunostaining was performed using Pearson simple correlation.

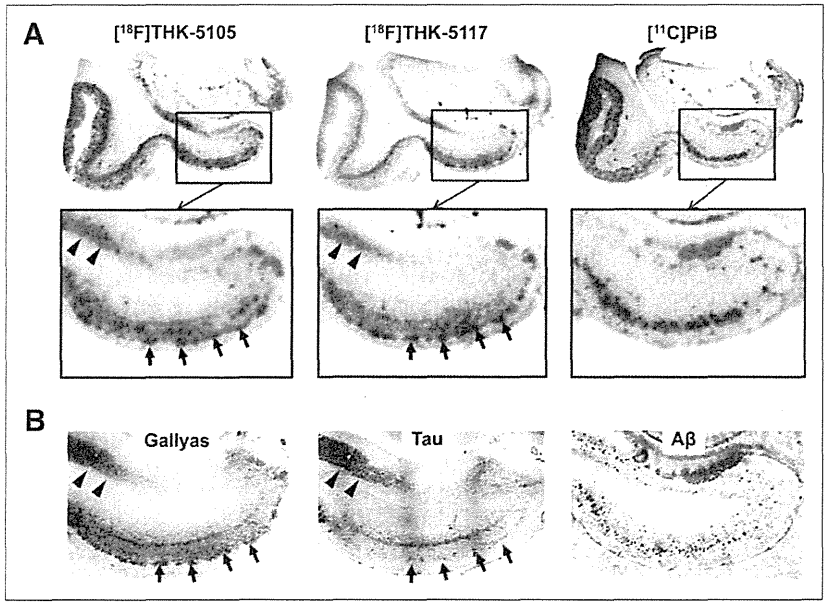

FIGURE 5. (A) Autoradiographic images of ^{18}F-THK-5105, ^{18}F-THK-5117, and ^{11}C-PiB binding in mesial temporal section from AD patient. (B) Gallyas–Braak silver staining (left) and immunostaining with anti-tau (center) and anti-Aβ (right) antibodies in adjacent brain sections. Arrowheads = CA1 area of hippocampus; longer arrows = entorhinal cortex.

Biodistribution in Mice

The experimental protocol of animal study was approved by the Ethics Committee of Tohoku University School of Medicine. ^{18}F-labeled tracers (1.1–6.3 MBq) were injected into the tail vein of male ICR mice (n = 20; mean weight, 28–32 g). Mice were then sacrificed by decapitation at 2, 10, 30, 60, and 120 min after injection. The brain, blood, liver, kidney, and femur were removed and weighed, and radioactivity was counted with an automatic γ-counter. The percentage injected dose per gram of tissue (%ID/g) was calculated by comparing tissue counts to tissue weight. Each %ID/g value is expressed as a mean ± SD of 4 separate experiments.

Animal Toxicity Studies

A 14-d toxicity study with intravenous administration of a single dose of THK-5105 and THK-5117 was performed using Sprague–Dawley rats and ICR mice. Briefly, the study included 3 groups of male and female rats and mice that were administered 0 (group 1), 0.1 (group 2), and 1 (group 3) mg/kg of test article (10% dimethylsulfoxide/90% distilled water) per rat or mouse by intravenous injection on study day 1. The study included clinical observations plus body weight measurements for a 14-d observation period. Hematology and pathologic examinations were conducted on study days 2 and 15. Detailed necropsies with external examinations were also performed.

Receptor Binding Assays

Receptor binding screens were conducted by Sekisui Medical Inc. Binding inhibition effects of 1 μM THK-5105 and THK-5117 were evaluated in competitive radioligand assays against 60 common neurotransmitter receptors, ion channels, and transporters. Percentage inhibition ratios were calculated by the following equation: inhibition ratio (%) = $[1 - (B - N)/(B_0 - N)] \times 100$, where N is the nonspecific bound radioactivity, and B and B_0 are the bound radioactivity in the presence and absence of tested compounds, respectively. Data are expressed as the mean values of duplicate samples.

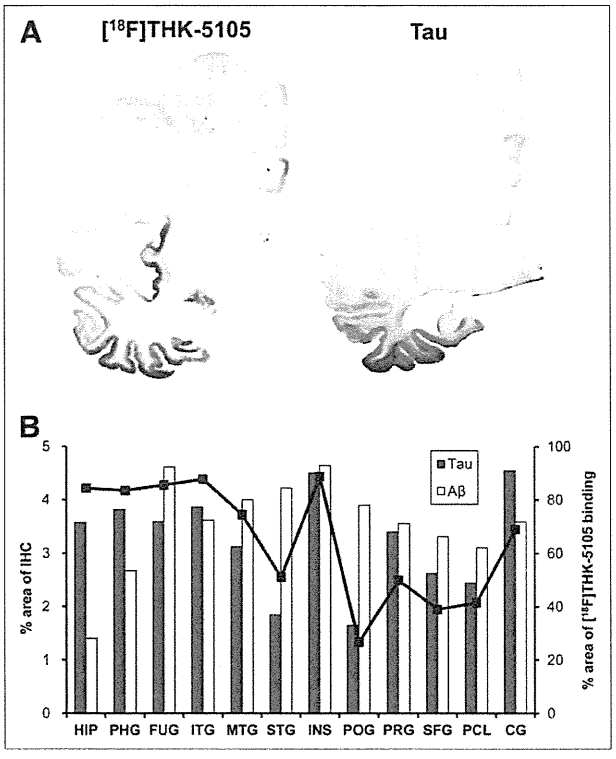

FIGURE 6. (A) Autoradiography of hemibrain sections from AD patient with ^{18}F-THK-5105 and tau immunostaining in neighboring section. (B) Region-of-interest analysis indicated that percentage areas of ^{18}F-THK-5105 binding (line plots) were significantly correlated with percentage areas of tau immunostaining (gray bars) but not with that of Aβ immunostaining (white bars). CG = cingulate gyrus; HIP = hippocampus; FUG = fusiform gyrus; IHC = immunohistochemistry; INS = insula; ITG = inferior temporal gyrus; MTG = middle temporal gyrus; PCL = paracentral lobule; PHG = parahippocampal gyrus; POG = postcentral gyrus; PRG = precentral gyrus; SFG = superior frontal gyrus; STG = superior temporal gyrus.

RESULTS

Radiosynthesis

All radiolabeled compounds were obtained in greater than 97% radiochemical purities after HPLC purification. The decay-corrected average radiochemical yields of ^{18}F-THK-523, ^{18}F-THK-5105, ^{18}F-THK-5116, ^{18}F-THK-5117, and ^{18}F-FDDNP were 58%, 48%, 41%, 48%, and 22%, respectively. The specific activities of ^{18}F-labeded compounds ranged from 37 to 110 GBq/μmol, corrected at the end of synthesis. The mean specific activity of ^{11}C-PiB was 35 GBq/μmol.

In Vitro Binding Assays

The binding properties of phenylquinoline derivatives to tau fibrils was investigated and compared with Aβ1–42 fibrils. Although only a single class of ^{18}F-THK-5105 binding sites was identified on Aβ1–42 fibrils, 2 classes of ^{18}F-THK-5105 binding sites were identified on K18Δ280-tau fibrils. As shown in Table 2, the K_d for the first class of K18Δ280-tau binding sites was 1.45 nM, indicating higher binding affinity to tau fibrils than to Aβ1–42 fibrils (K_d = 35.9 nM). Further, competitive binding assays with ^{18}F-THK-5105 displayed high binding affinity of phenylquinoline derivatives to tau fibrils (Fig. 3). The K_i for THK-5117 was 10.5 nM, indicating that THK-5117 has higher binding affinity for tau fibrils than THK-523 (K_i = 59.3 nM). In contrast, the K_i for FDDNP was 263 nM. In binding assays using mesial temporal brain homogenates containing a high density of tau (1,075 pmol/g) and moderate density of Aβ (434 pmol/g), both ^{18}F-THK-5105 (K_d = 2.63 nM; B_{max} = 358 pmol/g of tissue) and ^{18}F-THK-5117 (K_d = 5.19 nM; B_{max} = 338 pmol/g of tissue) showed higher affinity for mesial temporal brain homogenates than ^{18}F-THK-523 (K_d = 86.5 nM; B_{max} = 647.1 pmol/g of tissue) (Supplemental Fig. 1; supplemental materials are available online only at http://jnm.snmjournals.org).

Tissue Staining and Autoradiography

The selective binding ability of the compounds was further examined using AD brain sections. The fluorescent compound THK-5105 clearly stained NFTs and neuropil threads in the hippocampal section of an AD patient (Fig. 4A). Selective binding of this compound with tau pathology was confirmed by comparing with the results of tau immunohistochemistry for the same sections (Fig. 4B). In contrast, SPs were faintly stained with THK-5105. Further, we compared findings of THK-5105 staining with those of Gallyas–Braak silver staining, a conventional technique used to visualize tau pathology in the AD brain (Figs. 4C and 4D), and the binding of THK-5105 to NFTs and neuropil threads was confirmed. The images of staining with THK-5116 and THK-5117 were similar to those with THK-5105 (data not shown).

To investigate the binding ability of ^{18}F-THK-5105 and ^{18}F-THK-5117 to NFTs at tracer doses, in vitro autoradiography was performed in postmortem AD brain sections, and the findings were compared with Gallyas–Braak staining and immunohistochemistry. In the mesial temporal sections, laminar distributions of ^{18}F-THK-5105 and ^{18}F-THK-5117 were observed in the deep layer of gray matter (Fig. 5A). A high density of tracer accumulation was observed in the CA1 area of the hippocampus, which is reported as the most frequent site for NFTs in AD (*31*). These tracer distributions coincided with Gallyas–Braak staining and tau immunostaining (Fig. 5B) but not with the distribution of ^{11}C-PiB (Fig. 5A) and Aβ immunostaining (Fig. 5B). In contrast, no significant accumulation of ^{18}F-THK-5105 and ^{18}F-THK-5117 was observed in the hippocampus of the healthy control subject (Supplemental Fig. 2). ^{18}F-THK-5116 failed to give a specific signal in the AD brain sections (data not shown).

To further assess the regional differences of tracer binding in the AD brain, ^{18}F-THK-5105 autoradiography was conducted using AD hemibrain sections and compared with the Aβ PET tracer ^{11}C-PiB (*32*). ^{18}F-THK-5105 densely accumulated in the gray matter of the hippocampus, parahippocampal gyrus, fusiform gyrus, inferior and middle temporal gyri, insula, and cingulate gyrus (Fig. 6A), regions known for the abundance of tau pathology in AD (*33*). In contrast, tracer binding in the parietal areas was modest. The pattern of tracer distribution correlated with the known distribution of tau pathology (Fig. 6A) but not with the known distribution of Aβ or the binding of ^{11}C-PiB (data not shown). In addition, quantitative analyses of these images demonstrated a significant correlation of ^{18}F-THK-5105 binding with tau immunostained areas but not with the areas of Aβ immunostaining (Fig. 6B; Supplemental Fig. 3). In contrast, ^{11}C-PiB bindings showed a good correlation with Aβ deposition but not with tau deposition (Supplemental Fig. 3).

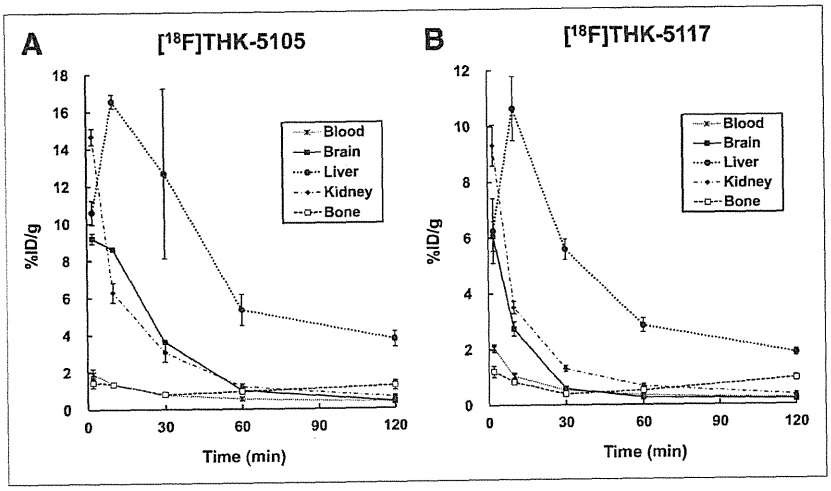

FIGURE 7. Time–activity curves after intravenous administration of ^{18}F-THK-5105 (A) and ^{18}F-THK-5117 (B) in mice.

Pharmacokinetics in Mice

All tested compounds exhibited sufficient amounts of tracer uptake in the mouse brain immediately after intravenous administration. Compared with ^{18}F-THK-523, new compounds showed significantly higher brain uptake at 2 min after injection (Table 1). ^{18}F-THK-5105 showed the highest brain uptake. In addition, clearance of these derivatives from normal brain tissue was faster than that of ^{18}F-THK-523 and ^{18}F-FDDNP (Table 1). The brain uptake ratio at 2 versus 60 min was highest for ^{18}F-THK-5117, followed by ^{18}F-THK-5105, ^{18}F-THK-5116, ^{18}F-FDDNP, and ^{18}F-THK-523. After injection of ^{18}F-THK-5105 and ^{18}F-THK-5117, the regional tracer uptake in the liver was highest at 10 min after injection, and the tracer was then slowly washed out from the body (Fig. 7). Compared with ^{18}F-THK-5105, ^{18}F-THK-5117 tended to have faster clearance from the brain, blood, liver, and kidney. No remarkable accumulation of ^{18}F-THK-5105 and ^{18}F-THK-5117 was observed in the bone.

Animal Toxicity Studies

A single intravenous administration of THK-5105 and THK-5117 at 1 mg/kg, equivalent to 100,000-fold the intended clinical dose for humans, caused no systemic toxicity in rats or mice. There were no unscheduled deaths or morbidity detected in this study. During the experimental period, the body weight of all animals increased normally, and no treatment-related changes were noted in any animals. There were no major clinical, biochemical, or histopathologic findings associated with the administration of THK-5105 and THK-5117.

Receptor Binding Assays

Binding inhibition of THK-5105 and THK-5117 was assessed in competitive radioligand binding assays against 60 common neurotransmitter receptors, ion channels, and transporters. As a result, no remarkable inhibition (<50%) was observed for various receptors, ion channels, and transporters at 1-μM concentrations of THK-5105 and THK-5117.

DISCUSSION

These findings suggest that ^{18}F-THK-5105 and ^{18}F-THK-5117 are promising candidates as tau imaging PET probes. Although previous saturation analysis showed the high binding affinity of ^{18}F-THK-523 for tau fibrils (K_d = 1.67 nM), the current competition assay demonstrated relatively lower binding affinity of THK-523 for tau fibrils (K_i = 59.3 nM) than THK-5105 (K_i = 7.8 nM) and THK-5117 (K_i = 10.5 nM). ^{18}F-THK-5105 showed higher affinity for tau pathology than for Aβ pathology in AD brain sections. Most amyloid imaging agents potentially bind to both tau and Aβ fibrils, because both protein fibrils share a common β-sheet secondary structure. To ensure the binding specificity of these compounds as tau-selective PET probes, the binding affinity to Aβ fibrils should be below the in vivo detection threshold. In vitro binding assays indicated that the binding affinity of ^{18}F-THK-5105 for Aβ fibrils (K_d = 35.9 nM) was 25 times lower than for tau fibrils (K_d = 1.45 nM). This K_d would allow selective detection of tau pathology, because the usual required K_d values for imaging Aβ are below 20 nM (*34*). However, the required K_d value for imaging tau deposits is still unknown. Considering that the concentrations of tau are about an order of magnitude lower than those of Aβ, the K_d value for tau should be well below 20 nM, in the low nanomolar range, to allow sensitive detection of tau pathology. In that respect, the binding affinities of both ^{18}F-THK-5105 and ^{18}F-THK-5117 to tau fibrils may be sufficient for in vivo detection of tau pathology in the brain. However, in vitro binding assay data should be carefully interpreted, because the structural conformation of synthetic tau fibrils does not fully correlate with the structure of NFTs and neuropil threads in the human brain. Actually, ^{18}F-THK-523 showed substantially lower affinity for AD brain homogenates (Kd = 86.5 nM) than for synthetic tau protein fibrils (Kd = 1.67 nM) (*15*). In the future, in vitro binding data should be compared with in vivo PET data to determine the required K_d value for in vivo tau detection.

In vitro assays using human brain samples are considered more reliable for evaluating the binding selectivity of radiotracers to tau and Aβ pathology at tracer doses. Autoradiography studies using human brain sections demonstrated the preferential binding of ^{18}F-THK-5105 and ^{18}F-THK-5117 to tau protein deposits in the AD brain. We observed a high density of ^{18}F-THK-5105 and ^{18}F-THK-5117 binding in the CA1 region of AD hippocampus, which contained substantial amounts of NFTs and neuropil threads. In addition, these tracers clearly visualized the laminar distribution of tau in the pri-α layer of the transentorhinal and temporal cortices, which is typically observed in the AD brain (*5*). The distribution pattern of THK tracer binding in AD brains was different from that of the Aβ imaging probe PiB and BF-227, which showed diffuse punctate distribution in broad neocortical gray matter and less tracer distribution in the mesial temporal region. These findings strongly suggest that binding properties of ^{18}F-THK-5105 and ^{18}F-THK-5117 are different from those of currently available Aβ PET probes. Compared with ^{18}F-THK-523 (*17*), both ^{18}F-THK-5105 and ^{18}F-THK-5117 showed higher contrast of tau pathology in autoradiographic images. These findings most likely reflect the increased binding affinity to tau by methylation of the amino group, as indicated by in vitro binding assays.

Similar findings were previously reported in an arylbenzothiazole derivative (*35*). Compared with ^{18}F-THK-5105, ^{18}F-THK-5117 showed lesser tracer binding in the gray matter containing high density of Aβ plaques, suggesting low binding affinity to Aβ and high selectivity to tau. ^{18}F-THK-5105 tends to show higher signals in the gray matter, and some of the images of ^{18}F-THK-5105 binding showed the patchy pattern as observed for ^{11}C-PiB binding. One possible reason for this is the binding of ^{18}F-THK-5105 to tau protein in dystrophic neurites. Another possible reason is binding of ^{18}F-THK-5105 to Aβ fibrils. However, the latter explanation seems unlikely given that ^{18}F-THK-5105 binding, as clearly shown in Figure 6, was correlated with tau, and not Aβ, deposits.

In vitro binding assays using AD brain homogenates are generally used to measure the binding affinity of Aβ imaging radiotracers to SPs or NFTs and the number of binding sites in real AD pathology (*36*). For most of the useful Aβ imaging radiotracers, the reported K_d or K_i values for neocortical brain samples are below 10 nM (*36,37*). In this study, the K_d values for high-affinity sites of AD mesial temporal homogenates were 2.63 nM for ^{18}F-THK-5105 and 5.19 nM for ^{18}F-THK-5117. These binding affinities were higher than that for ^{18}F-THK-523 and appear to be sufficient for the in vivo detection of AD pathology in the mesial temporal region at tracer doses. Furthermore, the B_{max}/K_d ratios of ^{18}F-THK-5105 and ^{18}F-THK-5117 for AD brain homogenates were 136.1 and 65.1, respectively, which fulfills the criteria (B_{max}/K_d ratio $>$ 10) for a good neuroimaging agent (*35*).

The optimization of pharmacokinetics is an important aspect in the development of a PET tracer (*38*). ^{18}F-THK-5105, ^{18}F-THK-5116, and ^{18}F-THK-5117 fulfilled the criteria of appropriate log P value (log P = 1–3) for brain entry (*39*). In mice, these tracers showed sufficient brain uptake and rapid washout from normal brain tissue. ^{18}F-THK-5105 and ^{18}F-THK-5117 exhibited high initial brain uptake in normal mice (>6 %ID/g at 2 min). These values, which are equivalent to over 100% injected dose index in a 25-g mouse, meet the prerequisites for useful PET imaging agents (*34*). The 2- to 60-min ratio of radioactivity concentrations for ^{18}F-THK-5117 was 23.1, indicating faster washout from normal brain for these compounds than for other currently available ^{18}F-labeled tracers such as ^{18}F-FDDNP (2.91), ^{18}F-florbetaben (4.83) (*40*), and ^{18}F-florbetapir (3.90) (*37*). Compared with ^{18}F-THK-523, ^{18}F-THK-5116 washed out faster from normal brain tissue of mice, indicating that the hydroxylation of the fluoroalkoxy group improves pharmacokinetics in mice. However ^{18}F-THK-5116 is not a suitable compound for clinical application, because of its lower initial brain uptake and binding affinity than the other 2 compounds.

CONCLUSION

^{18}F-THK-5105 and ^{18}F-THK-5117 should be considered as promising candidates for PET tau imaging radiotracers. Future clinical studies will clarify the usefulness of these radiotracers for the early detection of AD tau pathology.

DISCLOSURE

The costs of publication of this article were defrayed in part by the payment of page charges. Therefore, and solely to indicate this fact, this article is hereby marked "advertisement" in accordance with 18 USC section 1734. This study was supported by the research fund from GE Healthcare; the Industrial Technology Research Grant Program of the NEDO in Japan (09E51025a); Health and Labor Sciences Research grants from the Ministry of Health, Labor, and Welfare of Japan; and a Grant-in-Aid for Scientific Research (B) (23390297) and "Japan Advanced Molecular Imaging Program (J-AMP)" of the Ministry of Education, Culture, Sports, Science and Technology (MEXT), Japan. No other potential conflict of interest relevant to this article was reported.

REFERENCES

1. Organisation for Economic Co-operation and Development (OECD). *Understanding the Brain: The Birth of a Learning Science*. Paris, France: OECD Publishing, 2007.
2. Hardy J, Selkoe DJ. The amyloid hypothesis of Alzheimer's disease: progress and problems on the road to therapeutics. *Science*. 2002;297:353–356.
3. Lichtenberg B, Mandelkow EM, Hagestedt T, Mandelkow E. Structure and elasticity of microtubule-associated protein tau. *Nature*. 1988;334:359–362.
4. Holzer M, Holzapfel HP, Zedlick D, Bruckner MK, Arendt T. Abnormally phosphorylated tau protein in Alzheimer's disease: heterogeneity of individual regional distribution and relationship to clinical severity. *Neuroscience*. 1994;63:499–516.
5. Braak H, Braak E. Neuropathological stageing of Alzheimer-related changes. *Acta Neuropathol*. 1991;82:239–259.
6. Bondareff W, Mountjoy CQ, Roth M, Hauser DL. Neurofibrillary degeneration and neuronal loss in Alzheimer's disease. *Neurobiol Aging*. 1989;10:709–715.
7. Bobinski M, Wegiel J, Wisniewski HM, et al. Neurofibrillary pathology: correlation with hippocampal formation atrophy in Alzheimer disease. *Neurobiol Aging*. 1996;17:909–919.
8. Guillozet AL, Weintraub S, Mash DC, Mesulam MM. Neurofibrillary tangles, amyloid, and memory in aging and mild cognitive impairment. *Arch Neurol*. 2003;60:729–736.
9. Gómez-Isla T, Price JL, McKeel DW Jr., Morris JC, Growdon JH, Hyman BT. Profound loss of layer II entorhinal cortex neurons occurs in very mild Alzheimer's disease. *J Neurosci*. 1996;16:4491–4500.
10. Okamura N, Suemoto T, Furumoto S, et al. Quinoline and benzimidazole derivatives: candidate probes for in vivo imaging of tau pathology in Alzheimer's disease. *J Neurosci*. 2005;25:10857–10862.
11. Rojo LE, Alzate-Morales J, Saavedra IN, Davies P, Maccioni RB. Selective interaction of lansoprazole and astemizole with tau polymers: potential new clinical use in diagnosis of Alzheimer's disease. *J Alzheimers Dis*. 2010;19:573–589.
12. Ono M, Hayashi S, Matsumura K, et al. Rhodanine and thiohydantoin derivatives for detecting tau pathology in Alzheimer's brains. *ACS Chem Neurosci*. 2011;2:269–275.
13. Jensen JR, Cisek K, Funk KE, Naphade S, Schafer KN, Kuret J. Research towards tau imaging. *J Alzheimers Dis*. 2011;26(suppl 3):147–157.
14. Zhang W, Arteaga J, Cashion DK, et al. A highly selective and specific PET tracer for imaging of tau pathologies. *J Alzheimers Dis*. 2012;31:601–612.
15. Fodero-Tavoletti MT, Okamura N, Furumoto S, et al. ^{18}F-THK523: a novel in vivo tau imaging ligand for Alzheimer's disease. *Brain*. 2011;134:1089–1100.
16. Villemagne VL, Furumoto S, Fodero-Tavoletti MT, et al. The challenges of tau imaging. *Future Neurol*. 2012;7:409–421.
17. Harada R, Okamura N, Furumoto S, et al. Comparison of the binding characteristics of [^{18}F]THK-523 and other amyloid imaging tracers to Alzheimer's disease pathology. *Eur J Nucl Med Mol Imaging*. 2013;40:125–132.
18. Small GW, Agdeppa ED, Kepe V, Satyamurthy N, Huang SC, Barrio JR. In vivo brain imaging of tangle burden in humans. *J Mol Neurosci*. 2002;19:323–327.
19. Agdeppa ED, Kepe V, Liu J, et al. Binding characteristics of radiofluorinated 6-dialkylamino-2-naphthylethylidene derivatives as positron emission tomography imaging probes for beta-amyloid plaques in Alzheimer's disease. *J Neurosci*. 2001;21:RC189.
20. Thompson PW, Ye L, Morgenstern JL, et al. Interaction of the amyloid imaging tracer FDDNP with hallmark Alzheimer's disease pathologies. *J Neurochem*. 2009;109:623–630.
21. Tolboom N, Yaqub M, van der Flier WM, et al. Detection of Alzheimer pathology in vivo using both ^{11}C-PIB and ^{18}F-FDDNP PET. *J Nucl Med*. 2009;50:191–197.
22. Shoghi-Jadid K, Small GW, Agdeppa ED, et al. Localization of neurofibrillary tangles and beta-amyloid plaques in the brains of living patients with Alzheimer disease. *Am J Geriatr Psychiatry*. 2002;10:24–35.

23. Näslund J, Haroutunian V, Mohs R, et al. Correlation between elevated levels of amyloid beta-peptide in the brain and cognitive decline. *JAMA.* 2000;283: 1571–1577.
24. Mukaetova-Ladinska EB, Harrington CR, Roth M, Wischik CM. Biochemical and anatomical redistribution of tau protein in Alzheimer's disease. *Am J Pathol.* 1993;143:565–578.
25. Liu J, Kepe V, Zabjek A, et al. High-yield, automated radiosynthesis of 2-(1-{6-[(2-[^{18}F]fluoroethyl)(methyl)amino]-2-naphthyl}ethylidene)malononitrile ([^{18}F] FDDNP) ready for animal or human administration. *Mol Imaging Biol.* 2007;9:6–16.
26. Fodero-Tavoletti MT, Mulligan RS, Okamura N, et al. In vitro characterisation of BF227 binding to alpha-synuclein/Lewy bodies. *Eur J Pharmacol.* 2009;617:54–58.
27. Wilson AA, Garcia A, Chestakova A, Kung H, Houle S. A rapid one-step radiosynthesis of the beta-amyloid imaging radiotracer N-methyl-[C-11]2-(4′-methylaminophenyl)-6-hydroxybenzothiazole ([C-11]-6-OH-BTA-1). *J Labelled Comp Radiopharm.* 2004;47:679–682.
28. Cheng Y, Prusoff WH. Relationship between the inhibition constant (Ki) and the concentration of inhibitor which causes 50 per cent inhibition (IC50) of an enzymatic reaction. *Biochem Pharmacol.* 1973;22:3099–3108.
29. Okamura N, Suemoto T, Shimadzu H, et al. Styrylbenzoxazole derivatives for in vivo imaging of amyloid plaques in the brain. *J Neurosci.* 2004;24: 2535–2541.
30. Ikeda K, Akiyama H, Kondo H, Haga C. A study of dementia with argyrophilic grains. Possible cytoskeletal abnormality in dendrospinal portion of neurons and oligodendroglia. *Acta Neuropathol.* 1995;89:409–414.
31. Bouras C, Hof PR, Giannakopoulos P, Michel JP, Morrison JH. Regional distribution of neurofibrillary tangles and senile plaques in the cerebral cortex of elderly patients: a quantitative evaluation of a one-year autopsy population from a geriatric hospital. *Cereb Cortex.* 1994;4:138–150.
32. Kudo Y, Okamura N, Furumoto S, et al. 2-(2-[2-Dimethylaminothiazol-5-yl] ethenyl)-6- (2-[fluoro]ethoxy)benzoxazole: a novel PET agent for in vivo detection of dense amyloid plaques in Alzheimer's disease patients. *J Nucl Med.* 2007;48:553–561.
33. Braak H, Alafuzoff I, Arzberger T, Kretzschmar H, Del Tredici K. Staging of Alzheimer disease-associated neurofibrillary pathology using paraffin sections and immunocytochemistry. *Acta Neuropathol.* 2006;112:389–404.
34. Mathis CA, Wang Y, Klunk WE. Imaging beta-amyloid plaques and neurofibrillary tangles in the aging human brain. *Curr Pharm Des.* 2004;10:1469–1492.
35. Mathis CA, Wang Y, Holt DP, Huang GF, Debnath ML, Klunk WE. Synthesis and evaluation of ^{11}C-labeled 6-substituted 2-arylbenzothiazoles as amyloid imaging agents. *J Med Chem.* 2003;46:2740–2754.
36. Klunk WE, Wang Y, Huang GF, et al. The binding of 2-(4′-methylaminophenyl) benzothiazole to postmortem brain homogenates is dominated by the amyloid component. *J Neurosci.* 2003;23:2086–2092.
37. Choi SR, Golding G, Zhuang Z, et al. Preclinical properties of ^{18}F-AV-45: a PET agent for Abeta plaques in the brain. *J Nucl Med.* 2009;50:1887–1894.
38. Furumoto S, Okamura N, Iwata R, Yanai K, Arai H, Kudo Y. Recent advances in the development of amyloid imaging agents. *Curr Top Med Chem.* 2007;7:1773–1789.
39. Waterhouse RN. Determination of lipophilicity and its use as a predictor of blood-brain barrier penetration of molecular imaging agents. *Mol Imaging Biol.* 2003;5:376–389.
40. Zhang W, Oya S, Kung MP, Hou C, Maier DL, Kung HF. F-18 Polyethyleneglycol stilbenes as PET imaging agents targeting Abeta aggregates in the brain. *Nucl Med Biol.* 2005;32:799–809.

Eur J Nucl Med Mol Imaging (2013) 40:125–132
DOI 10.1007/s00259-012-2261-2

ORIGINAL ARTICLE

Comparison of the binding characteristics of [^{18}F]THK-523 and other amyloid imaging tracers to Alzheimer's disease pathology

Ryuichi Harada · Nobuyuki Okamura · Shozo Furumoto · Tetsuro Tago · Masahiro Maruyama · Makoto Higuchi · Takeo Yoshikawa · Hiroyuki Arai · Ren Iwata · Yukitsuka Kudo · Kazuhiko Yanai

Received: 1 May 2012 / Accepted: 21 September 2012 / Published online: 26 October 2012

Abstract
Purpose Extensive deposition of senile plaques and neurofibrillary tangles in the brain is a pathological hallmark of Alzheimer's disease (AD). Although several PET imaging agents have been developed for in vivo detection of senile plaques, no PET probe is currently available for selective detection of neurofibrillary tangles in the living human brain. Recently, [^{18}F]THK-523 was developed as a potential in vivo imaging probe for tau pathology. The purpose of this study was to compare the binding properties of [^{18}F]THK-523 and other amyloid imaging agents, including PiB, BF-227 and FDDNP, to synthetic protein fibrils and human brain tissue.
Methods In vitro radioligand binding assays were conducted using synthetic amyloid β_{42} and K18ΔK280-tau fibrils. Nonspecific binding was determined by the addition of unlabelled compounds at a concentration of 2 μM. To examine radioligand binding to neuropathological lesions, in vitro autoradiography was conducted using sections of AD brain.
Results [^{18}F]THK-523 showed higher affinity for tau fibrils than for Aβ fibrils, whereas the other probes showed a higher affinity for Aβ fibrils. The autoradiographic analysis indicated that [^{18}F]THK-523 accumulated in the regions containing a high density of tau protein deposits. Conversely, PiB and BF-227 accumulated in the regions containing a high density of Aβ plaques.
Conclusion These findings suggest that the unique binding profile of [^{18}F]THK-523 can be used to identify tau deposits in AD brain.

Keywords PET probes · Tau · Amyloid · Alzheimer's disease

Electronic supplementary material The online version of this article (doi:10.1007/s00259-012-2261-2) contains supplementary material, which is available to authorized users.

R. Harada · N. Okamura (✉) · S. Furumoto · T. Yoshikawa · K. Yanai
Department of Pharmacology,
Tohoku University School of Medicine,
2-1, Seiryo-machi, Aoba-ku,
Sendai 980-8575, Japan
e-mail: nookamura@med.tohoku.ac.jp

S. Furumoto · T. Tago · R. Iwata
Division of Radiopharmaceutical Chemistry,
Cyclotron and Radioisotope Center, Tohoku University,
Sendai, Japan

M. Maruyama · M. Higuchi
Molecular Imaging Center, National Institute
of Radiological Sciences,
Chiba, Japan

H. Arai
Department of Geriatrics and Gerontology, Institute of
Development, Aging and Cancer, Tohoku University,
Sendai, Japan

Y. Kudo
Innovation of New Biomedical Engineering Center,
Tohoku University,
Sendai, Japan

Introduction

Senile plaques and neurofibrillary tangles (NFTs) composed of amyloid-β (Aβ) peptides and aggregated tau proteins, respectively, are the pathological hallmarks of

Alzheimer's disease (AD). In vivo amyloid imaging techniques have received a lot of attention for their promise in presymptomatic detection of Aβ pathology [1]. Recently, several β-sheet binding radiotracers have been developed as PET amyloid imaging agents [2]. Among them, ^{18}F-labelled 2-(1-{6-[(2-fluoroethyl(methyl)amino)-2-naphthyl)ethylidene)malononitrile ([^{18}F]FDDNP) was the first PET probe to be applied to clinical PET imaging in patients with AD [3]. This tracer demonstrated higher regional uptake in the medial temporal lobe and neocortex, and was claimed to bind to Aβ and tau pathological lesions [3]. Subsequently, ^{11}C-labelled 2-[4′-(methylamino)phenyl]-6-hydroxybenzothiazole ([^{11}C]PiB) and 2-(2-[dimethylaminothiazole-5-yl]ethenyl)-6-(2-[fluoro]ethoxy)benzoxazole ([^{11}C]BF-227) were also developed as amyloid imaging radiotracers. These tracers bind to Aβ fibrils with high affinity [4] and have demonstrated a significantly higher retention in the neocortical areas of brains of AD patients than of healthy controls [5, 6]. Furthermore, post-mortem analysis of AD patients who had undergone [^{11}C]PiB PET imaging before death suggested a strong correlation between in vivo PiB binding and regional distribution of Aβ plaques [7].

Amyloid imaging with PET can detect AD pathology in its preclinical stage [8]. However, amyloid deposition as assessed by [^{11}C]PiB PET correlates poorly with cognitive impairment in AD [9, 10], whereas deposition of tau in the medial temporal cortex is closely associated with neuronal death in this region. Selective tau imaging would provide important information about the tau pathophysiological features in AD, allowing correlation of brain tau load with cognitive decline, monitoring of disease progression and evaluation of therapeutic efficacy of newly developed therapies. Potential candidates for in vivo tau imaging agents include quinoline derivatives [11], and in a recent study, we found that one quinoline derivative, [^{18}F]THK-523, showed higher affinity for tau rather than amyloid fibrils. Furthermore, an autoradiography analysis indicated that this tracer binds specifically to tau deposits but not Aβ burden at tracer concentrations usually achieved during a PET scan [12].

The binding profiles of PiB, BF-227 and FDDNP to Aβ fibrils have been well described. Because tau, α-synuclein and prion fibrils, as well as Aβ fibrils, share a common β-sheet secondary structure, these compounds can potentially bind all these misfolded proteins. A previous study indicated that PiB binds to both Aβ and PHF tau pathology in vitro [13]. However, the binding occurs at higher concentrations than usually achieved in vivo during a PET scan. Furthermore, PET–pathology correlation studies have demonstrated that PiB binding reflects Aβ pathology [7, 14]. Newly developed ^{18}F-labelled amyloid PET tracers have similarly shown good correlation with Aβ plaque density [15, 16]. However, the binding affinity of these radiotracers for tau fibrils remains unknown and the binding properties of [^{18}F]THK-523 have not been directly compared with those of other amyloid PET agents. Here, we compared the binding affinity of [^{18}F]THK-523 to synthetic Aβ and tau protein fibrils as well as to senile plaques and NFTs in human brain samples with those of PiB, BF-227 and FDDNP, to characterize the binding properties of THK-523 and to obtain a better understanding of current and future PET data.

Materials and methods

Materials

The nonlabelled compounds PiB, BF-227, FDDNP, THK-523 (Fig. 1) and their precursors were custom-synthesized by Tanabe R&D Service (Osaka, Japan). Human $A\beta_{42}$ was purchased from Peptide Institute Inc. (Mino, Japan). Recombinant K18ΔK280-tau protein was obtained from Invitrogen (Tokyo, Japan).

Radiolabelling of PiB, BF-227, THK-523 and FDDNP

[^{3}H]PiB (specific activity 2.96 GBq/μmol) was purchased from American Radiolabeled Chemicals (St. Louis, MO). [^{11}C]PiB was radiolabelled using its precursor (2-(4-aminophenyl)-6-methoxymethoxybenzothiazole) and [^{11}C]methyl triflate, as

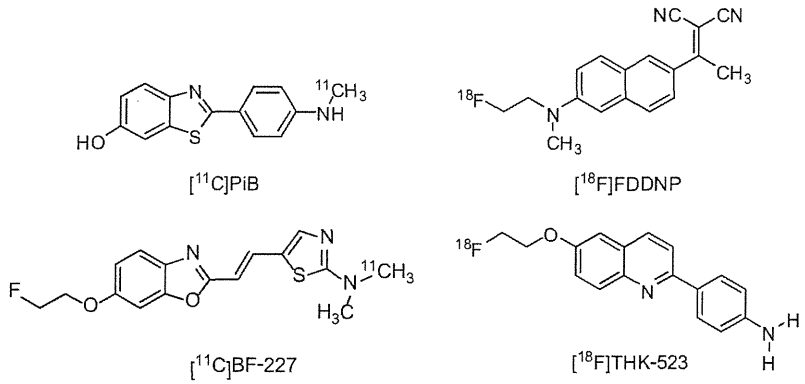

Fig. 1 Chemical structures of [^{11}C]PiB, [^{18}F]FDDNP, [^{11}C]BF-227 and [^{18}F]THK-523

previously described [17, 18]. The mean specific activity of [^{11}C]PiB was 34.6 GBq/μmol.

[^{18}F]BF-227 was synthesized by nucleophilic substitution of the tosylate precursor (2-[2-(2-dimethylaminothiazol-5-yl)ethenyl]-6-[2-(tosyloxy)ethoxy]benzoxazole. After a 10-min reaction at 110 °C, the crude mixture was partially purified on an activated Sep-Pak tC18 cartridge before being purified by semipreparative reverse-phase HPLC. Standard tC18 Sep-Pak reformulation produced [^{18}F]BF-227 in >95 % purity. The radiochemical yield was 12–19 % (non-decay-corrected), and the mean specific activity of [^{18}F]BF-227 was 163 GBq/μmol at the end of the synthesis. [^{11}C]BF-227 was synthesized using *N*-desmethylated derivatives as its precursor and [^{11}C]methyl triflate, as previously described [6]. The mean specific activity of [^{11}C]BF-227 was 136 GBq/μmol.

[^{18}F]THK-523 was synthesized by nucleophilic substitution of the tosylate precursor (2-(4-aminophenyl)-6-(2-tosyloxyethoxy)quinolone) as previously described [12]. The standard tC18 Sep-Pak reformulation produced [^{18}F]THK-523 in >95 % purity. The radiochemical yield was 38–49 % (non-decay-corrected), and the mean specific activity of [^{18}F]THK-523 was 68 GBq/μmol at the end of the synthesis.

[^{18}F]FDDNP was radiolabelled by the nucleophilic substitution of the tosylate precursor (2-{[6-(2,2-dicyano-1-methylvinyl)-2-naphthyl](methyl)amino}ethyl-4-methylbenzenesulphonate) as previously described [19]. After a 15-min reaction at 95 °C, the crude mixture was partially purified on an activated Sep-Pak tC18 cartridge before being purified by semipreparative reverse-phase HPLC. Standard tC18 Sep-Pak reformulation produced [^{18}F]FDDNP in >95 % purity. The radiochemical yield was 12–19 % (non-decay-corrected), and the mean specific activity of [^{18}F]FDDNP was 27 GBq/μmol at the end of the synthesis. All analysis HPLC chromatograms are shown in the Supplementary figure.

In vitro radioligand binding assays

Synthetic $A\beta_{42}$ fibrils and K18ΔK280-tau fibrils were prepared as previously described [12]. For in vitro binding assays, synthetic $A\beta_{42}$ or K18ΔK280 fibrils (200 nM) were incubated with increasing concentrations of [^{3}H]PiB and ^{18}F-labelled compounds (0.5–200 nM). To account for nonspecific binding of [^{3}H]PiB and ^{18}F-labelled compounds, the above-mentioned reactions were performed in triplicate in the presence of each unlabelled compound at a concentration of 2 μM.

The binding reactions were incubated for 1 h for the ^{18}F-labelled compounds and 3 h for [^{3}H]PiB at room temperature, in 200 μL of assay buffer (Dulbecco's PBS, 0.1 % BSA). Separation of bound from free radioactivity was achieved by filtration under reduced pressure (MultiScreen HTS Vacuum Manifold, MultiScreen HTS 96-well 0.65-μm filtration plate; Millipore, Billerica, MA). The filters were washed three times with 200-μL assay buffer, and the filters containing the bound ^{18}F-labelled compounds were then assayed for radioactivity in a γ counter (AccuFLEX γ7000, Aloka, Tokyo, Japan). The filters containing [^{3}H]PiB were incubated in 2 mL of scintillation fluid (Aquasol-2; PerkinElmer, Boston, MA), and the radioactivity of ^{3}H was counted using a β counter (LS6500 liquid scintillation counter; Beckman Coulter, Brea, CA). The binding data were analysed with curve-fitting software that calculated the K_D and B_{max} using nonlinear regression (GraphPad Prism version 5.0; GraphPad Software, San Diego, CA).

Autoradiography, immunohistochemistry and Gallyas silver staining

Demographics of post-mortem brain samples are shown in Table 1. The frontal and medial temporal brain sections (6 μm thick) of three AD patients were incubated with 1.0 MBq/mL ^{11}C-labelled and ^{18}F-labelled compounds at room temperature for 10 min and then washed briefly with water and 50 % ethanol. After drying, the labelled sections were exposed to a BAS-III imaging plate (Fuji Film, Tokyo, Japan) overnight. The autoradiographic images were obtained using a BAS-5000 phosphoimaging instrument (Fuji Film) with a spatial resolution of 25×25 μm. The adjacent sections were immunostained using AT8 anti-tau monoclonal antibody (diluted 1:20; Innogenetics, Ghent, Belgium) and 6F/3D (diluted 1:50; Dako, Glostrup, Denmark). The adjacent sections were also stained by the Gallyas-Braak method, which has been reported to be NFT-specific [20].

Results

Binding affinity for synthetic Aβ and tau fibrils

To characterize the binding properties of THK-523, PiB, BF-227 and FDDNP, in vitro radioligand binding assays for synthetic $A\beta_{42}$ and truncated tau construct (K18ΔK280) fibrils were performed under the same experimental conditions. Truncated tau construct (K18ΔK280) consists of the four repeat regions (244–372) but lacking lysine 280 (ΔK280) observed in FTLD-17 familial mutation.

Table 1 Demographics of brain samples used in this study

Brain no.	Age (years)	Sex	Post-mortem interval (h)
AD1	76	F	16
AD2	82	F	17
AD3	92	F	8.5

K18ΔK280 tau aggregates exhibit the similar characteristic as PHF-tau from AD brain [21]. In addition, K18ΔK280 tau forms aggregates quickly without cofactor such as heparin [22]. Thus, we used K18ΔK280 fibrils for the in vitro binding assays. Our analysis indicated that [^{18}F]THK-523 had a higher binding affinity for tau fibrils (K_{D1} = 1.99 ± 0.21 nM, B_{max1} = 1.22 ± 0.24 pmol THK-523/nmol K18ΔK280-tau) than for $A\beta_{42}$ fibrils (K_{D1} = 30.3 ± 3.91 nM, B_{max1} = 12.6 ± 0.45 pmol THK-523/nmol $A\beta_{42}$), which was similar to previously published data [12]. On the other hand, [^{3}H]PiB bound to $A\beta_{42}$ fibrils with high affinity (K_{D1} = 0.84 ± 0.18 nM, B_{max1} = 0.44 ± 0.07 pmol PiB/nmol $A\beta_{42}$). [^{3}H]PiB also showed two binding sites for K18ΔK280-tau fibrils, but with a lower affinity (K_{D1} = 6.39 ± 1.63 nM, B_{max1} = 1.38 ± 0.48 pmol PiB/nmol K18ΔK280) than [^{18}F]THK-523. [^{18}F]BF-227 showed a high binding affinity for $A\beta_{42}$ fibrils (K_{D1} = 1.72 ± 0.83 nM, B_{max1} = 0.50 ± 0.14 pmol BF-227/nmol $A\beta_{42}$), similar to our previous report [23], but showed a lower affinity for tau fibrils (K_D = 30.2 ± 2.29 nM, B_{max} = 10.7 ± 0.24 pmol BF-227/nmol K18ΔK280-tau). [^{18}F]BF-227 had an approximately 20-fold higher affinity for the first class of $A\beta_{42}$ binding sites compared with tau fibrils. Only one class of [^{18}F]FDDNP binding site was identified on the $A\beta_{42}$ (K_D = 5.52 ± 1.97 nM, B_{max} = 0.277 ± 0.06 pmol FDDNP/nmol $A\beta_{42}$) and K18ΔK280 tau fibrils (K_D = 36.7 ± 11.6 nM, B_{max} = 2.14 ± 0.46 pmol FDDNP/nmol K18ΔK280-tau). These results suggest that [^{18}F]FDDNP binds $A\beta_{42}$ fibrils with lower affinity than [^{3}H]PiB and [^{18}F]BF-227. Furthermore, [^{18}F]FDDNP had an approximately sevenfold higher affinity for $A\beta_{42}$ fibrils than for tau fibrils. These binding profiles are significantly different from that of [^{18}F]THK-523 (Table 2).

In vitro autoradiography of human brain sections

To further assess the binding selectivity of [^{18}F]THK-523, autoradiographic images of the frontal (Fig. 2) and medial temporal (Fig. 3) brain sections from three AD patients, using [^{18}F]THK-523, [^{11}C]PiB and [^{11}C]BF-227, were compared. While Aβ plaques in the frontal grey matter were labelled with [^{11}C]PiB (Fig. 2a–c) and [^{11}C]BF-227 (Fig. 2g–i), the binding of [^{18}F]THK-523 in the frontal grey matter (Fig. 2m–o) was considerably lower. In the medial temporal brain sections, [^{11}C]PiB (Fig. 3a–c) and [^{11}C]BF-227 (Fig. 3g–i) did not accumulate in the hippocampal CA1 area, whereas [^{18}F]THK-523 (Fig. 3m–o) did accumulate in this area (Fig. 3m–o). The presence of a high density of tau and a low density of Aβ in this area was confirmed by immunohistochemistry (Fig. 3d–f, j–l). Furthermore, the band-like distribution of [^{18}F]THK-523 in the inner layer of the temporal grey matter was similar to the distribution of tau (Fig. 3j–l). In the high-magnification images of case AD3 (Fig. 3p–v), the distribution of [^{18}F]THK-523 closely resembled Gallyas silver staining and tau immunostaining. [^{18}F]THK-523 binding was observed in the areas showing a high density of NFTs in the hippocampal CA1, the layer pre-α and pri-α in the entorhinal cortex (ERC) (Fig. 3p, q, r, t). Intriguingly, [^{18}F]THK-523 labelling in the layer pre-α of the ERC corresponded to Gallyas silver staining better than tau immunostaining, suggesting the preferential binding of [^{18}F]THK-523 to extracellular tau deposits that were clearly visualized by Gallyas silver staining [25]. In contrast to [^{18}F]THK-523, the distribution of [^{11}C]PiB was similar to that of Aβ immunohistochemistry (Fig 3q, u, v). [^{11}C]PiB binding corresponded to the formation of amyloid in the parvopyramidal layer of the presubicular area and in the layers pre-β and pre-γ of the ERC (Fig. 3s, v) [26].

Discussion

In the study reported here, we for the first time directly compared the binding properties of the novel quinoline derivative THK-523 and other amyloid PET probes. Our data suggest the potential utility of THK-523 for the selective detection of PHF-tau in the living human brain, which has not previously been achieved. The autoradiographic images of sections from AD brains revealed that [^{18}F]THK-523 successfully labelled PHF-tau deposits but did not label Aβ deposits in the frontal and temporal cortices. These findings suggest that [^{18}F]THK-523 is a promising

Table 2 K_D and B_{max} values of [^{3}H]PiB, [^{18}F]BF-227, [^{18}F]FDDNP and [^{18}F]THK-523 for K18ΔK280-tau and $A\beta_{42}$ fibrils

Compound	K18ΔK280 fibrils				$A\beta_{42}$ fibrils			
	K_{D1}	B_{max1}	K_{D2}	B_{max2}	K_{D1}	B_{max1}	K_{D2}	B_{max2}
[^{18}F]THK-523	1.99±0.21	1.22±0.24	50.7±2.73	4.55±0.74	30.3±3.91	12.6±0.45	–	–
[^{18}F]BF-227	30.2±2.29	10.7±0.24	–	–	1.72±0.83	0.50±0.14	56.1±25.1	13.4±4.37
[^{18}F]FDDNP	36.7±11.6	2.14±0.46	–	–	5.52±1.97	0.277±0.06	–	–
[^{3}H]PiB	6.39±1.63	1.38±0.48	304±77.4	20.6±11.2	0.84±0.18	0.44±0.07	60.6±8.32	26.1±8.57

K_D values are in nanomoles, and B_{max} values are in picomoles compound per nanomole fibrils (n=3).

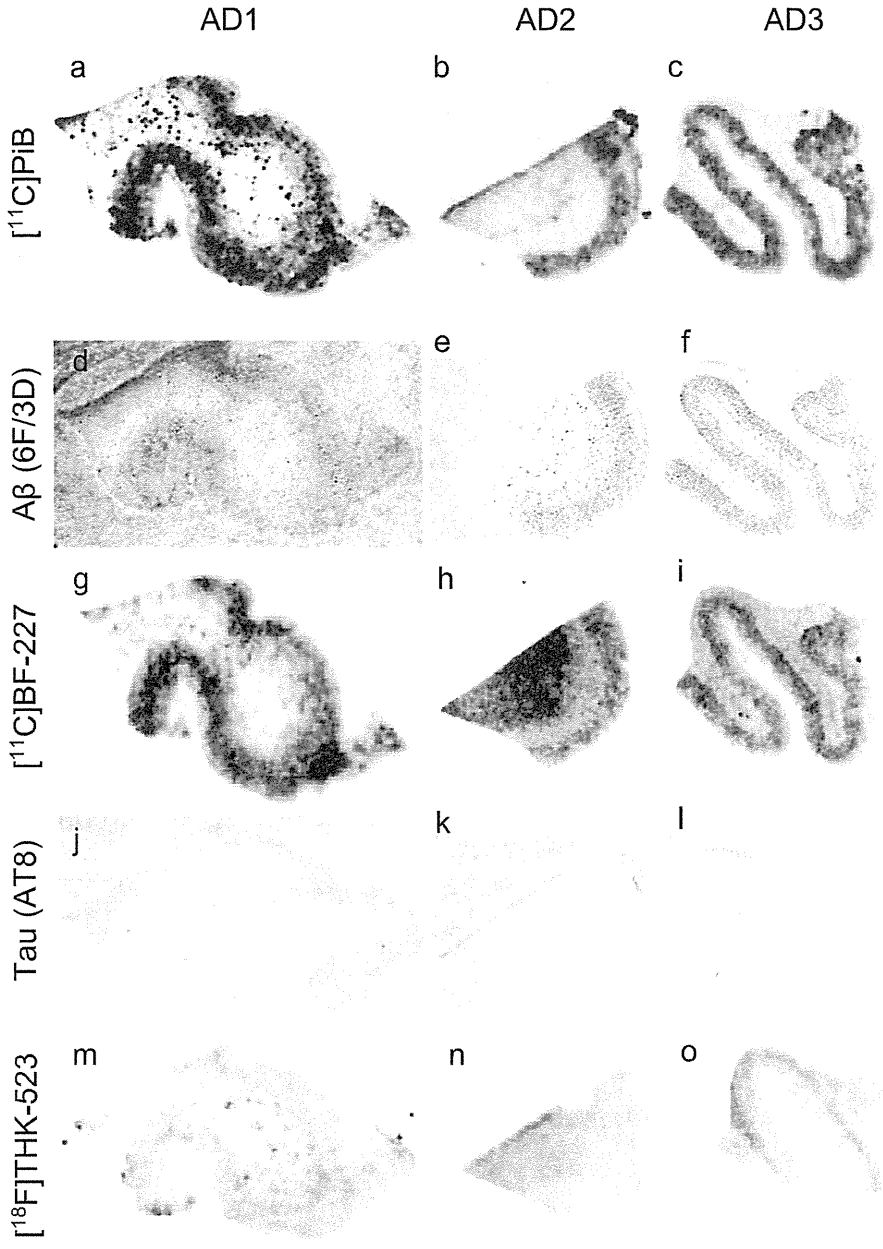

Fig. 2 Comparison of [^{11}C]PiB, [^{11}C]BF-227 and [^{18}F]THK-523 autoradiography with the Aβ and tau immunostaining in sections of the frontal brain from three patients with AD (*AD1*, *AD2*, *AD3*). Both [^{11}C]PiB (**a–c**) and [^{11}C]BF-227 (**g–i**) showed dense accumulation in the grey matter, closely resembling the pattern of Aβ immunohistochemistry using the 6F/3D antibody (**d–f**). [^{18}F]THK-523 (**m–o**) did not accumulate in the grey matter, which was correlated with no marked staining with anti-tau antibody AT8 (**j–l**)

candidate as a tau imaging tracer, and could also be a lead compound for future development of tau-selective radiotracers. We speculate that [^{18}F]THK-523 would show retention in tau-rich brain regions if administered to AD patients. However, the specific signal of [^{18}F]THK-523 might be lower than those of PiB and BF-227 owing to the lower amount of tau deposits in the neocortex of AD patients [27]. Further compound optimization may be required to achieve higher contrast imaging of PHF-tau deposits.

In in vitro saturation binding studies [^{18}F]THK-523 bound with higher affinity to tau fibrils (K_{D1} 1.99 nM) than to $A\beta_{42}$ fibrils (K_{D1} 30.3 nM), whereas PiB and BF-227 showed the opposite binding characteristics. [^{3}H]PiB bound with higher affinity to $A\beta_{42}$ fibrils (K_{D1} 0.84 nM) than to tau fibrils (K_{D1} 6.39 nM), similar to previous reports [7, 28, 29], and [^{18}F]BF-227 had more than a tenfold higher affinity for $A\beta_{42}$ fibrils (K_{D1} 1.72 nM) than for tau fibrils (K18ΔK280; K_{D1} 30.2 nM). Autoradiographic images of sections of AD brain revealed that [^{11}C]PiB and [^{11}C]BF-227 accumulated in the grey matter of the neocortex, which closely resembled the staining pattern of Aβ immunohistochemistry. A previous study suggested that [^{3}H]PiB labelled NFTs at tracer concentrations usually achieved during a PET scan [13]. However, another study showed no binding of the PiB derivative [^{3}H]BTA-1 to

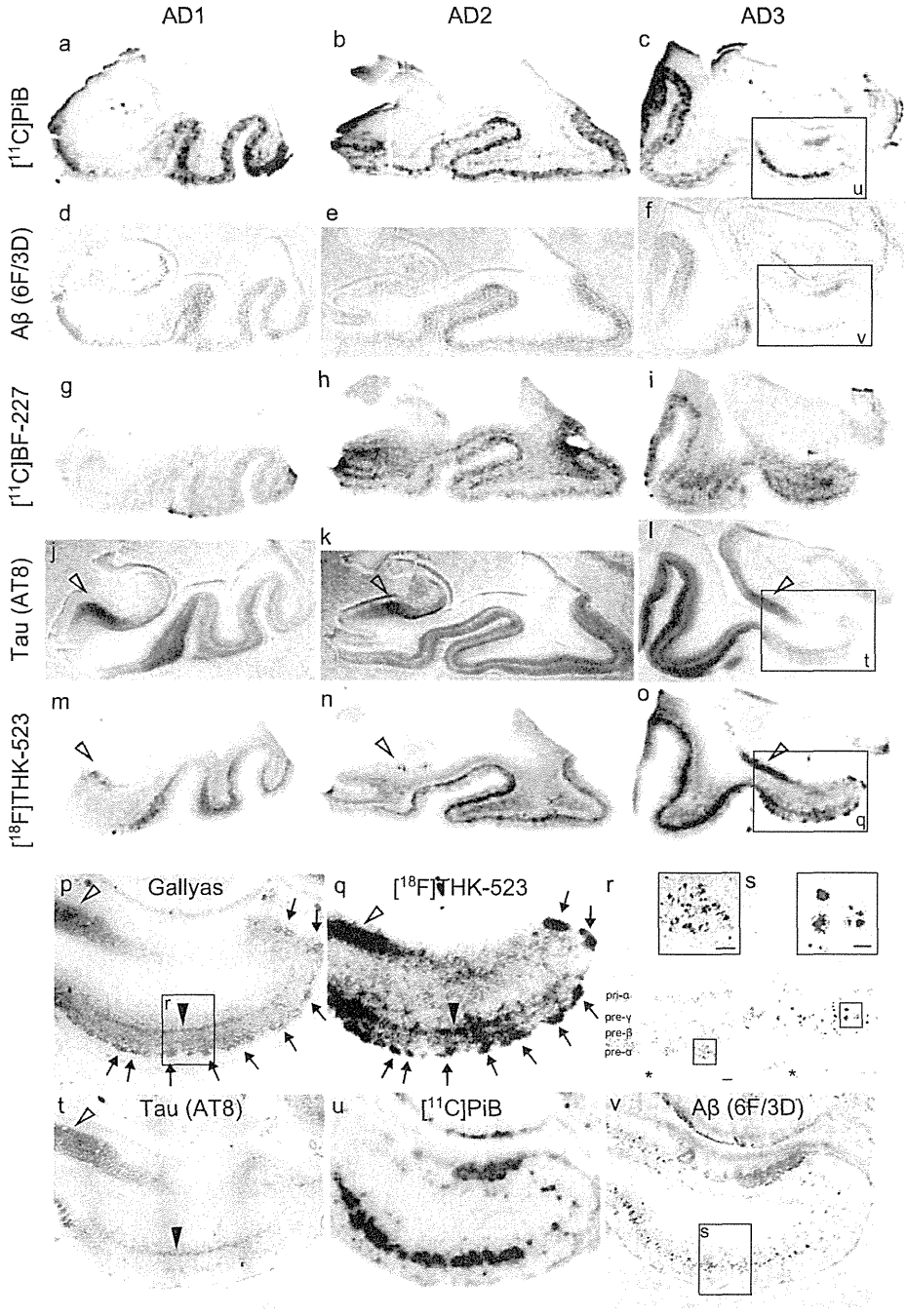

Fig. 3 Comparison of [^{11}C]PiB, [^{11}C]BF-227 and [^{18}F]THK-523 autoradiography with Aβ and tau immunostaining images in sections of the medial temporal brain from three patients with AD (*AD1*, *AD2*, *AD3*). [^{11}C]PiB (**a**–**c**) and [^{11}C]BF-227 (**g**–**i**) do not accumulate in the hippocampal CA1 area which contains a low density of Aβ (**d**–**f**). In contrast, accumulation of [^{18}F]THK-523 is observed in the hippocampal CA1 area (**m**–**o**, *arrowheads*), which closely resembles AT8 immunoreactivity (**j**–**l**, *arrowheads*). In addition, the band-like labelling pattern of [^{18}F]THK-523 in the inner layer of temporal cortex (**m**–**o**) is closely similar to that of AT8 immunostaining (**j**–**l**). **p**–**v** High magnification images of the medial temporal sections from patient AD3. Many clusters of [^{18}F]THK-523 binding in the ERC are consistent with Gallyas silver staining (**p**, **q**, *arrows*). **r** Close-up image from **p**. Numerous NFTs are located in the layer pre-α of the ERC (**r** *inset*). The band-like distribution of [^{18}F]THK-523 in the layer pri-α of the ERC also resembles the labelling pattern of Gallyas silver staining (**p**, *filled arrowhead*) as well as AT8 immunoreactivity (**t**, *filled arrowhead*). [^{11}C]PiB binding (**u**) is also present in the ERC, but obviously different from [^{18}F]THK-523 binding (**q**) and similar to the 6F/3D immunostaining pattern (**v**). Lake-like amyloid in the presubicular region (**v**) is labelled with [^{11}C]PiB, but not with [^{18}F]THK-523. **s** Close-up image from **v**. Aβ plaques (**s** *inset*) located in the layer pre-β and pre-γ are intensely labelled with [^{11}C]PiB (**u**). *Asterisks* in **r** and **s** denote the same large blood vessel. *Scale bar* 100 μm

plaque-free and NFT-rich ERC homogenates, despite the high amount of [^{3}H]BTA-1 binding to frontal cortex homogenates containing high levels of neuritic plaques [30]. Autoradiographic and immunohistochemical analyses indicated that PiB predominantly binds to senile plaques but not to NFTs. These findings are consistent with the findings from clinical PiB-PET studies showing no remarkable PiB retention in the medial temporal cortex of AD patients [7].

Another radiotracer, [^{18}F]FDDNP, has been reported to detect Aβ and tau pathological lesions in AD patients [3]. Previous clinical PET studies have shown higher cortical uptake of [^{18}F]FDDNP in the lateral and medial temporal lobes of AD subjects [3, 5]. Furthermore, a multitracer PET study of [^{11}C]PiB and [^{18}F]FDDNP has shown significant retention of FDDNP in the medial temporal cortex, albeit no remarkable retention of PiB in the same region [31]. However, in vitro binding studies have shown the limited binding affinity of [^{3}H]FDDNP to AD pathological lesions [24], and a previous autoradiographic analysis has suggested that [^{3}H]FDDNP does not significantly label any region in AD brain [24]. Previous in vitro binding studies additionally showed the binding affinity of FDDNP for $A\beta_{40}$ fibrils (K_D 0.12, 85 nM) [19, 24], but the binding affinity for tau fibrils was not reported. Here, we showed that the binding affinity of [^{18}F]FDDNP for tau fibrils (K_{D1} 36.7 nM) was similar to that of [^{18}F]BF-227 (K_{D1} 30.2 nM), but much higher than that of [^{18}F]THK-523 (K_{D1} 1.99 nM).

In conclusion, the binding profiles of [^{18}F]THK-523, [^{11}C]PiB, [^{18}F]BF-227, and [^{18}F]FDDNP were compared using in vitro saturation binding assays and autoradiography of sections of AD brain. These data suggest that [^{18}F]THK-523 shows a binding preference for tau protein fibrils. Therefore, [^{18}F]THK-523 is a candidate as a radiotracer to identify tau protein deposits and a lead compound for future tracer development. Ongoing clinical trials will clarify the clinical utility of this tracer and its derivatives for tau imaging in vivo.

Acknowledgments This study was supported by the Industrial Technology Research Grant Program of the NEDO in Japan, Health and Labor Sciences Research Grants from the Ministry of Health, Labor, and Welfare of Japan, and Grant-in-Aid for Scientific Research (B) (23390297).

References

1. Nordberg A, Rinne JO, Kadir A, Langstrom B. The use of PET in Alzheimer disease. Nat Rev Neurol. 2010;6:78–87. doi:10.1038/nrneurol.2009.217.
2. Furumoto S, Okamura N, Iwata R, Yanai K, Arai H, Kudo Y. Recent advances in the development of amyloid imaging agents. Curr Top Med Chem. 2007;7:1773–89.
3. Shoghi-Jadid K, Small GW, Agdeppa ED, Kepe V, Ercoli LM, Siddarth P, et al. Localization of neurofibrillary tangles and beta-amyloid plaques in the brains of living patients with Alzheimer disease. Am J Geriatr Psychiatry. 2002;10:24–35.
4. Mathis CA, Wang Y, Holt DP, Huang GF, Debnath ML, Klunk WE. Synthesis and evaluation of 11C-labeled 6-substituted 2-arylbenzothiazoles as amyloid imaging agents. J Med Chem. 2003;46:2740–54. doi:10.1021/jm030026b.
5. Klunk WE, Engler H, Nordberg A, Wang Y, Blomqvist G, Holt DP, et al. Imaging brain amyloid in Alzheimer's disease with Pittsburgh Compound-B. Ann Neurol. 2004;55:306–19. doi:10.1002/ana.20009.
6. Kudo Y, Okamura N, Furumoto S, Tashiro M, Furukawa K, Maruyama M, et al. 2-(2-[2-Dimethylaminothiazol-5-yl]ethenyl)-6- (2-[fluoro]ethoxy)benzoxazole: a novel PET agent for in vivo detection of dense amyloid plaques in Alzheimer's disease patients. J Nucl Med. 2007;48:553–61.
7. Ikonomovic MD, Klunk WE, Abrahamson EE, Mathis CA, Price JC, Tsopelas ND, et al. Post-mortem correlates of in vivo PiB-PET amyloid imaging in a typical case of Alzheimer's disease. Brain. 2008;131:1630–45. doi:10.1093/brain/awn016.
8. Sperling RA, Aisen PS, Beckett LA, Bennett DA, Craft S, Fagan AM, et al. Toward defining the preclinical stages of Alzheimer's disease: recommendations from the National Institute on Aging-Alzheimer's Association workgroups on diagnostic guidelines for Alzheimer's disease. Alzheimers Dement. 2011;7:280–92. doi:10.1016/j.jalz.2011.03.003.
9. Jack Jr CR, Knopman DS, Jagust WJ, Shaw LM, Aisen PS, Weiner MW, et al. Hypothetical model of dynamic biomarkers of the Alzheimer's pathological cascade. Lancet Neurol. 2010;9:119–28. doi:10.1016/S1474-4422(09)70299-6.
10. Pike KE, Savage G, Villemagne VL, Ng S, Moss SA, Maruff P, et al. Beta-amyloid imaging and memory in non-demented individuals: evidence for preclinical Alzheimer's disease. Brain. 2007;130:2837–44. doi:10.1093/brain/awm238.
11. Okamura N, Suemoto T, Furumoto S, Suzuki M, Shimadzu H, Akatsu H, et al. Quinoline and benzimidazole derivatives: candidate probes for in vivo imaging of tau pathology in Alzheimer's disease. J Neurosci. 2005;25:10857–62. doi:10.1523/JNEUROSCI.1738-05.2005.
12. Fodero-Tavoletti MT, Okamura N, Furumoto S, Mulligan RS, Connor AR, McLean CA, et al. 18F-THK523: a novel in vivo tau imaging ligand for Alzheimer's disease. Brain. 2011;134:1089–100. doi:10.1093/Brain/Awr038.
13. Lockhart A, Lamb JR, Osredkar T, Sue LI, Joyce JN, Ye L, et al. PIB is a non-specific imaging marker of amyloid-beta (Abeta) peptide-related cerebral amyloidosis. Brain. 2007;130:2607–15. doi:10.1093/brain/awm191.
14. Burack MA, Hartlein J, Flores HP, Taylor-Reinwald L, Perlmutter JS, Cairns NJ. In vivo amyloid imaging in autopsy-confirmed Parkinson disease with dementia. Neurology. 2010;74:77–84. doi:10.1212/WNL.0b013e3181c7da8e.
15. Clark CM, Schneider JA, Bedell BJ, Beach TG, Bilker WB, Mintun MA, et al. Use of florbetapir-PET for imaging beta-amyloid pathology. JAMA. 2011;305:275–83. doi:10.1001/jama.2010.2008.
16. Wong DF, Moghekar AR, Rigamonti D, Brasic JR, Rousset O, Willis W, et al. An in vivo evaluation of cerebral cortical amyloid with [(18)F]Flutemetamol using positron emission tomography compared with parietal biopsy samples in living normal pressure hydrocephalus patients. Mol Imaging Biol. 2012. doi:10.1007/s11307-012-0583-x.
17. Maeda J, Ji B, Irie T, Tomiyama T, Maruyama M, Okauchi T, et al. Longitudinal, quantitative assessment of amyloid, neuroinflammation, and anti-amyloid treatment in a living mouse model of Alzheimer's disease enabled by positron emission tomography. J Neurosci. 2007;27:10957–68. doi:10.1523/JNEUROSCI.0673-07.2007.

18. Manook A, Yousefi BH, Willuweit A, Platzer S, Reder S, Voss A, et al. Small-animal PET imaging of amyloid-beta plaques with [11C]PiB and its multi-modal validation in an APP/PS1 mouse model of Alzheimer's disease. PLoS One. 2012;7:e31310. doi:10.1371/journal.pone.0031310.
19. Agdeppa ED, Kepe V, Liu J, Flores-Torres S, Satyamurthy N, Petric A, et al. Binding characteristics of radiofluorinated 6-dialkylamino-2-naphthylethylidene derivatives as positron emission tomography imaging probes for beta-amyloid plaques in Alzheimer's disease. J Neurosci. 2001;21:RC189.
20. Gallyas F. Silver staining of Alzheimer's neurofibrillary changes by means of physical development. Acta Morphol Acad Sci Hung. 1971;19:1–8.
21. Barghorn S, Davies P, Mandelkow E. Tau paired helical filaments from Alzheimer's disease brain and assembled in vitro are based on beta-structure in the core domain. Biochemistry. 2004;43:1694–703. doi:10.1021/bi0357006.
22. von Bergen M, Barghorn S, Muller SA, Pickhardt M, Biernat J, Mandelkow EM, et al. The core of tau-paired helical filaments studied by scanning transmission electron microscopy and limited proteolysis. Biochemistry. 2006;45:6446–57. doi:10.1021/bi052530j.
23. Fodero-Tavoletti MT, Mulligan RS, Okamura N, Furumoto S, Rowe CC, Kudo Y, et al. In vitro characterisation of BF227 binding to alpha-synuclein/Lewy bodies. Eur J Pharmacol. 2009;617:54–8. doi:10.1016/j.ejphar.2009.06.042.
24. Thompson PW, Ye L, Morgenstern JL, Sue L, Beach TG, Judd DJ, et al. Interaction of the amyloid imaging tracer FDDNP with hallmark Alzheimer's disease pathologies. J Neurochem. 2009;109:623–30. doi:10.1111/j.1471-4159.2009.05996.x.
25. Braak E, Braak H, Mandelkow EM. A sequence of cytoskeleton changes related to the formation of neurofibrillary tangles and neuropil threads. Acta Neuropathol. 1994;87:554–67.
26. Thal DR, Rub U, Schultz C, Sassin I, Ghebremedhin E, Del Tredici K, et al. Sequence of Abeta-protein deposition in the human medial temporal lobe. J Neuropathol Exp Neurol. 2000;59:733–48.
27. Villemagne VL, Furumoto S, Fodero-Tavoletti M, Harada R, Mulligan RS, Kudo Y, et al. The challenges of tau imaging. Future Neurol. 2012;7:409–21. doi:10.2217/fnl.12.34.
28. Fodero-Tavoletti MT, Smith DP, McLean CA, Adlard PA, Barnham KJ, Foster LE, et al. In vitro characterization of Pittsburgh compound-B binding to Lewy bodies. J Neurosci. 2007;27:10365–71. doi:10.1523/JNEUROSCI.0630-07.2007.
29. Klunk WE, Lopresti BJ, Ikonomovic MD, Lefterov IM, Koldamova RP, Abrahamson EE, et al. Binding of the positron emission tomography tracer Pittsburgh compound-B reflects the amount of amyloid-beta in Alzheimer's disease brain but not in transgenic mouse brain. J Neurosci. 2005;25:10598–606. doi:10.1523/JNEUROSCI.2990-05.2005.
30. Klunk WE, Wang Y, Huang GF, Debnath ML, Holt DP, Shao L, et al. The binding of 2-(4'-methylaminophenyl)benzothiazole to post-mortem brain homogenates is dominated by the amyloid component. J Neurosci. 2003;23:2086–92.
31. Shin J, Lee SY, Kim SH, Kim YB, Cho SJ. Multitracer PET imaging of amyloid plaques and neurofibrillary tangles in Alzheimer's disease. Neuroimage. 2008;43:236–44. doi:10.1016/j.neuroimage.2008.07.022.

Insights Imaging
DOI 10.1007/s13244-014-0312-x

PICTORIAL REVIEW

Imaging spectrum of sporadic cerebral amyloid angiopathy: multifaceted features of a single pathological condition

Keita Sakurai · Aya M. Tokumaru · Tomoya Nakatsuka · Shigeo Murayama · Shin Hasebe · Etsuko Imabayashi · Kazutomi Kanemaru · Masaki Takao · Hiroyuki Hatsuta · Kenji Ishii · Yuko Saito · Yuta Shibamoto · Noriyuki Matsukawa · Emiko Chikui · Hitoshi Terada

Received: 14 July 2013 / Revised: 23 December 2013 / Accepted: 13 January 2014

Abstract
Objectives Sporadic cerebral amyloid angiopathy (CAA) is common cause of cerebrovascular disorders that predominantly affect elderly patients. When symptomatic, cortical-subcortical intracerebral haemorrhage (ICH) in the elderly is the most well-known manifestation of CAA. Furthermore, the clinical presentation varies from a sudden neurological deficit to seizures, transient symptoms and acute progressive cognitive decline. Despite its clinical importance, this multifaceted nature poses a diagnostic challenge for radiologists. The aims of this study were to expound the characteristics of neuroimaging modalities, which cover a wide spectrum of CAA-related imaging findings, and to review the various abnormal findings for which CAA could be responsible.
Conclusions Radiologically, in addition to typical ICH, CAA leads to various types of abnormal findings, including microbleed, subarachnoid haemorrhage, superficial siderosis, microinfarction, reversible oedema, and irreversible leukoaraiosis. Taking into consideration the clinical importance of CAA-related disorders such as haemorrhagic risks and treatable oedema, it is necessary for radiologists to understand the wide spectrum of CAA-related imaging findings.
Teaching Points
- *To describe the characteristics of imaging modalities and findings of CAA-related disorders.*
- *MRI, especially gradient echo sequences, provides the useful information of CAA-related haemosiderin depositions.*
- *To understand the wide spectrum of CAA-related neuroimaging and clinical features is important.*

Keywords Cerebral amyloid angiopathy · Imaging · Subarachnoid haemorrhage · Microbleed · Superficial siderosis · CAA-related inflammation

K. Sakurai (✉) · A. M. Tokumaru · S. Hasebe · E. Imabayashi
Department of Diagnostic Radiology, Tokyo Metropolitan Medical Centre of Gerontology, 35-2 Sakaecho, Itabashi-ku, Tokyo 173-0015, Japan
e-mail: ksak666@yahoo.co.jp

T. Nakatsuka · H. Terada
Department of Radiology, Toho University Sakura Medical Centre, Sakura, Japan

S. Murayama · M. Takao · H. Hatsuta
Department of Neuropathology (the Brain Bank for Aging Research), Tokyo Metropolitan Geriatric Hospital, Tokyo Metropolitan Geriatric Hospital and Institute of Gerontology, Tokyo, Japan

K. Kanemaru
Department of Neurology, Tokyo Metropolitan Geriatric Hospital, Tokyo, Japan

K. Ishii
Positron Medical Centre, Tokyo Metropolitan Institute of Gerontology, Tokyo, Japan

Y. Saito
Department of Pathology and Laboratory Medicine, National Centre for Neurology and Psychiatry Hospital, Tokyo, Japan

Y. Shibamoto
Department of Radiology, Nagoya City University Graduate School of Medical Sciences, Nagoya, Japan

N. Matsukawa
Department of Neurology and Neuroscience, Nagoya City University Graduate School of Medical Sciences, Nagoya, Japan

E. Chikui
Department of Neurosurgery, Tokyo Metropolitan Geriatric Hospital, Tokyo, Japan

Published online: 12 February 2014

Introduction

Sporadic cerebral amyloid angiopathy (CAA) is a common small vessel disease of the brain, characterised by the progressive deposition of amyloid-β (Aβ) protein in the walls of small- to medium-sized arteries (up to about 2 mm in diameter), arterioles and capillaries in the cerebral cortex and overlying leptomeninges, preferentially affecting occipital regions for unclear reasons. In contrast to the amyloid plaques found in Alzheimer disease (AD), which are predominantly composed of the 42-amino-acid-residue fragment, the vascular amyloid in CAA is mostly composed of the more soluble, 40-amino-acid fragment, which suggests different pathophysiological mechanisms for pathological deposition [1]. Impairment in one or more elimination mechanisms may result in the accumulation of Aβ in the walls of small- and medium-sized leptomeningeal and cortical blood vessels. Upon autopsy, CAA may be found more commonly in women than in men. The incidence of CAA, like AD, is strongly age-dependent. Although found at autopsy in only 33 % of 60–70 year olds, the prevalence of age-related CAA increases to 75 % among those older than 90 years [2]. Despite its high prevalence, CAA remains an underestimated cause of cerebrovascular disease, both clinically and at imaging, in part because many patients are asymptomatic. When symptomatic, intracerebral haemorrhage (ICH) in the elderly is the most well-known manifestation. Furthermore, the clinical presentation varies from a sudden neurological deficit to seizures, transient symptoms and cognitive decline, including acute progressive dementia. However, these symptoms are not specific and are often not readily associated with CAA.

Radiologically, in addition to typical acute cortical-subcortical ICH, CAA leads to various types of abnormal findings, including chronic ICHs, microbleed (MB), subarachnoid haemorrhage (SAH), superficial siderosis (SS), microinfarction, reversible oedema and irreversible leukoaraiosis (Table 1) [3]. Taking into consideration the clinical importance of CAA-related haemorrhagic risks in the setting of antiplatelet, anticoagulation and thrombolysis therapies, as well as treatable oedema [3–6], it is necessary for radiologists to understand the wide spectrum of CAA-related imaging findings.

The aims of this study were the following: to expound the characteristics of neuroimaging modalities, including computed tomography (CT), magnetic resonance imaging (MRI) and positron emission tomography (PET), which cover a wide spectrum of CAA-related imaging findings, and to review the various abnormal findings for which CAA could be responsible. The recognition of wide-spectrum imaging findings can be useful for radiologists not only to raise the possibility of CAA but also to precisely comprehend the pathophysiology of CAA and management to improve the prognosis.

Neuroimaging modalities: critical roles in the diagnosis of CAA

CT

CT is the initial screening modality for patients with various symptoms, especially acute neurological deficits or transient ischaemic attack-like symptoms, which can allow rapid establishment of the presence or absence of ICHs and SAHs. CT can provide crucial information regarding the characteristics of these haemorrhagic conditions, including volume, shape and distribution. Additional CT angiography with intravenous contrast media is useful to exclude other pathological conditions (e.g. aneurysms, arteriovenous malformation, fistula and venous thrombosis) that could cause similar haemorrhagic complications.

On CT scan, cortical-subcortical ICHs without a history of hypertension and sulcal SAHs without a history of head trauma can be the findings suggestive of CAA. However, it is difficult to evaluate other findings, such as MBs and SS, which support the diagnosis of CAA. The disadvantage of CT is lower contrast resolution than MRI, which can depict acute cerebral infarctions, MBs and white matter lesions more clearly. In other words, CAA cannot be diagnosed by CT alone, but requires MRI sequences sensitive to susceptibility effects.

MRI

The important point of MRI in the diagnosis of CAA is to perform the proper sequences to cover a wide spectrum of CAA-related abnormal findings including not only haemorrhages but also oedemas and infarctions. Therefore, the standard imaging protocol should include at least the gradient-echo (GRE), fluid-attenuated inversion recovery (FLAIR) and diffusion-weighted imaging (DWI). The standard MRI protocol is shown in Table 2.

The optimal detection of haemorrhagic lesions, including MB and SS, depends on multiple MRI parameters, including pulse sequence, spatial resolution, echo time and field strength. Due to CAA-related pathological changes such as haemosiderin accumulations which lead to large variations in local magnetic fields and a local reduction in T2*, it is necessary to perform the GRE sequence, which is more sensitive to the magnetic susceptibility effect than turbo spin-echo sequences, in the diagnosis of CAA [7]. In the elderly, GRE sequences are essential to check for CAA-related MBs and/or SAH, which can potentially predict life-threatening lobar haemorrhages [8]. Compared with conventional 2D sequences, increasing spatial resolution (i.e. smaller voxel size) on 3D sequence improves the detection of MBs [9]. A longer echo time enables more efficient detection of MBs than a shorter one due to the blooming effect [9]. In addition to these parameters, higher susceptibility effects and increase of

Table 1 CAA-related abnormal imaging findings

Disease	Imaging findings	Recommended neuroimaging modality
ICH	Haematoma with distinctive cortical-subcortical distribution generally sparing the deep white matter and basal ganglia and brainstem	CT and MRI **MRI**; additional depiction of chronic haemosiderin depositions and MBs
MBs	Small round hypointense foci on MRI	MRI, especially susceptibility-weighted image
SAH	Supratentorial sulcal high attenuation/intensity, most frequently depicted around the precentral gyrus	CT and MRI **MRI**; additional depiction of MB and SS
SS	Hypointensity along the supratentorial cerebral sulcus on MRI	MRI, especially susceptibility-weighted image
CAA-related inflammation	Large confluent asymmetric abnormal attenuation/intensity mainly in the subcortical WM	CT and MRI **MRI**; additional evaluation of vasogenic oedema and other findings such as MB and SS
Leukoaraiosis	Low attenuation on CT and high intensity on FLAIR and T2W MRI mainly in the deep WM with sparing of the subcortical U fibres	CT and MRI MRI; depiction of leukoaraiosis clearer than CT
Microinfarction	Small ovoid or round high intensity of the subcortical and cortex on diffusion-weighted image	MRI, especially diffusion-weighted image

CAA cerebral amyloid angiopathy, *CT* computed tomography, *FLAIR* fluid-attenuated inversion recovery, *ICH* intracerebral haemorrhage, *MRI* magnetic resonance imaging, *MB* microbleed, *SAH* subarachnoid haemorrhage, *SS* superficial siderosis, *T2W* T2-weighted, *WM* white matter

signal-to-noise ratio with field strength improve the detection of MBs at a 3-T imager compared with a 1.5-T one [9]. Taking these parameters into consideration, it is reasonable to perform sophisticated 3D sequences with higher spatial resolution and longer echo time including a susceptibility-weighted image (SWI) and the principles of echo-shifting with a train of observations (PRESTO) image to detect MB and SS [9, 10]. Notably, SWI with smaller section thickness and higher magnetic field is currently the most sensitive technique to visualise MBs, which combines both magnitude information and phase information to accentuate the visibility of susceptible foci. These sequences can be of potential value in the evaluation of CAA patients (Fig. 1).

However, the GRE sequence is less sensitive than the FLAIR sequence for the detection of acute SAHs and parenchymal changes. The better lesion/tissue contrast achieved by the suppression of the signal intensity of cerebrospinal fluid (CSF) on the FLAIR sequence not only in the subarachnoid space, but also in the cerebral parenchyma can be especially useful for the evaluation of CAA-related white matter lesions and SAHs. In addition to these sequences, DWI with apparent diffusion coefficient (ADC) maps can be useful to distinguish CAA-related silent infarctions from other white matter lesions, including vasogenic oedema and leukoaraiosis [3, 5].

PET

Although clinical criteria based on MRI and CT findings have been validated for a pre-mortem diagnosis of CAA during life [11], this relies on detecting late manifestations of CAA-related vascular damage such as ICHs and MBs rather than the vascular amyloid itself. Therefore, these morphological

Table 2 Standard MRI protocol for the diagnosis of CAA

Sequence	Expected role for the diagnosis
Minimum required protocol	
T2*-weighted image	Depiction of haemosiderin depositions suggestive of chronic ICHs, MBs and SS
Fluid-attenuated inversion recovery image	Depiction of acute and subacute SAHs, and white matter signal changes
Diffusion-weighted image	Depiction of acute microinfarction Evaluation of vasogenic oedema due to CAA-related inflammation
Optional sequence for the diagnosis of CAA	
Susceptibility-weighted image	Depiction of haemosiderin depositions, clearer than T2*-weighted image
Additional sequences for differential diagnosis	
T1-weighted image	Depiction of T1 shortening due to methaemoglobin and melanin
Contrast-enhanced T1-weighted image	Differentiation between haemorrhagic tumours and other lesions
Magnetic resonance angiogram	Evaluation of vascular disorders such as vasculitis

CAA cerebral amyloid angiopathy, *ICH* intracerebral haemorrhage, *MB* microbleed, *MRI* magnetic resonance imaging, *SAH* subarachnoid haemorrhage, *SS* superficial siderosis

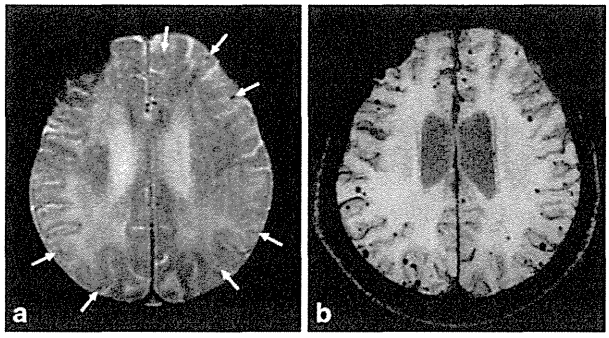

Fig. 1 Multiple MBs and CAA-related inflammation in a 78-year-old man. In addition to the right dominant diffuse white matter lesions, an axial GRE T2*-weighted image on the 1.5-T imager (**a**) revealed some cortical-subcortical hypointense foci suggestive of CAA-related MBs (*arrows*). Of note, more hypointense foci in the posterior dominant distribution were identified on the corresponding PRESTO image (**b**)

techniques cannot lead to a correct diagnosis in a definite proportion of CAA patients during life. However, an emerging functional technique, Pittsburgh compound B (PiB) PET imaging to measure the burden and location of fibrillar Aβ deposits, has recently been reported as a promising technique for CAA detection [12]. In addition to binding to fibrillar senile plaques, this radiotracer can clearly delineate the vascular amyloid before it triggers haemorrhagic complications or other overt small-vessel brain injuries, and can be a useful clue to diagnose not only AD but also CAA [13].

In the case of coexisting CAA and hypertension, the widespread involvement of arterioles by both types of arteriopathy likely causes the progression of small vessel disease and some overlap in the distribution of MBs [14]. In such cases, PiB-PET can provide a definite clue not only for the diagnosis of CAA but also the coexistence of hypertensive arteriopathy (Fig. 2). However, it is important to understand that PIB is a non-specific imaging marker of Aβ peptide-related cerebral amyloidosis. As previously mentioned, this tracer labels vascular as well as plaque Aβ; therefore, differentiating PiB signal caused by CAA from that caused by other kinds of plaques is difficult.

Representative imaging findings: multifaceted features of a single pathological condition

Lobar haemorrhage: a life-threatening sign

CAA is one of the most common causes of lobar ICHs in the elderly [15]. In addition to the advanced age, hypertension and minor head injuries may increase the risk of CAA-related ICHs [15, 16]. The clinical presentation of CAA-related ICH varies according to ICH size and location. Patients commonly present with an acute stroke syndrome with focal neurological deficits that may be associated with headache, vomiting, seizures and/or an altered level of consciousness. In the longer term, survivors of lobar ICHs are at a high risk of recurrence, especially with the presence of the ε2 or ε4 alleles of the apolipoprotein E gene (28 % cumulative recurrence rate at 2 years relative to 10 % in patients without either allele) [17].

Regardless of the size, CAA-related ICHs exhibit distinctive cortical-subcortical distributions that generally spare the deep white matter, basal ganglia and brainstem. This cortical-subcortical distribution of CAA-related ICHs has been correlated with the anatomical distribution of β-amyloid-containing vessels. Notably, haemorrhagic lesions are shown to be preferentially distributed in the temporal and occipital lobes, and are likely to cluster regardless of the lobes [18]. Comprehension of this characteristic distribution was validated by the Boston criteria, which are most commonly used and highly specific for the diagnosis of CAA (Table 3) [11, 19]. CAA-related macrohaemorrhages may be associated with subarachnoid, subdural or, less commonly, intraventricular haemorrhage (Figs. 3 and 4) [8]. Other neuroimaging findings suspicious for CAA-related ICHs include the multiplicity and recurrence of ICHs (Fig. 4). Recurrent haemorrhages are typically lobar, often in the same lobe as the initial CAA-related ICHs [18]. CT is sufficient to provide crucial information regarding the characteristics of acute CAA-related ICHs. However, MRI examinations including GRE sequences should be performed to evaluate chronic haemosiderin depositions and MBs, which can be useful to diagnose CAA.

Microbleeds: easily overlooked but a suggestive sign of CAA

This finding indicates previous extravasation of blood-related to bleeding-prone microangiopathy, including CAA and hypertensive arteriopathy (Fig. 5) [14]. In the pathological analysis of lobar MBs in CAA patients, various CAA-related pathologies, including acute microhaemorrhages, haemosiderin residua of old haemorrhages and small lacunes ringed by haemosiderin, are proved to produce signal voids on SWI [20]. MBs located in lobar regions may correlate with disease progression, recurrent ICH, and cognitive dysfunctions [21, 22]. Moreover, early recognition can be advantageous to patients on antiplatelet or thrombolysis therapy in that they are at an increased risk for subsequent and possibly fatal haemorrhages [4, 6].

MBs are typically defined on GRE sequences as small, well-demarcated, hypointense, rounded foci less than 5–10 mm in size, which are distinct from cortical vascular flow voids, leptomeningeal siderosis, or non-haemorrhagic subcortical mineralisation such as symmetrical hypointensities in the globus pallidus [21]. The presence of multiple, strictly lobar, cortical-subcortical MBs detected by GRE sequences has been shown to be highly specific for severe CAA in elderly patients with no other definite cause of ICH, such as trauma, ischaemic stroke, coagulopathy or excessive anticoagulation (probable

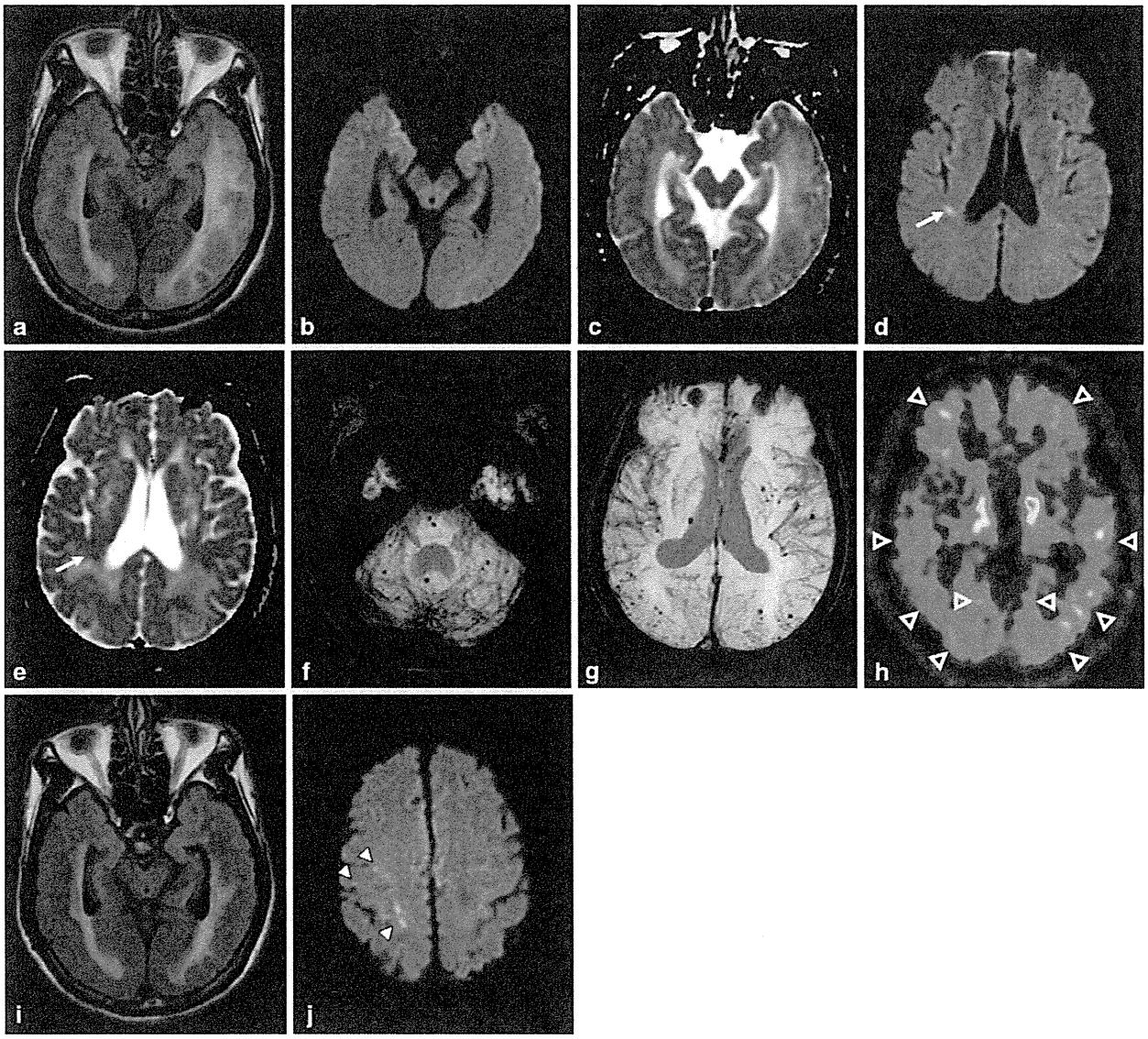

Fig. 2 CAA-related inflammation, MBs, and microinfarctions in a 72-year-old man. An axial FLAIR image (**a**) showed large confluent asymmetric hyperintense lesions, which involved not only the left dominant subcortical white matter but also the overlying left temporo-occipital cortices, with a mass effect. Low signal intensity on DWI (**b**) and increased diffusion on the ADC map (**c**) suggested vasogenic oedema. In addition to these white matter lesions, DWI (**d**) demonstrated a small right temporal hyperintense lesion (*arrow*) with corresponding decreased diffusion (*arrow*) on the ADC map (**e**) (*arrow*). This signal change indicated a relatively acute microinfarction. An axial 3D T2*-weighted image (**f**, **g**) revealed multiple MBs, which were distributed not only in the posterior dominant cortical-subcortical region but also in the left putamen, right thalamus, pons and cerebellum. A PiB-PET image (**h**) revealed the diffuse cortical accumulation, including the occipital lobes, higher than those of the cerebral white matter, which indicated the global PiB uptake (*open arrowheads*). These finding of MBs and PiB distribution suggested the coexistence of CAA and hypertensive arteriopathy. Two months after a course of intravenous steroid therapy, an improvement in the white matter lesions was identified on a FLAIR image (**i**). However, DWI (**j**) revealed new subcortical microinfarctions in the right frontal lobe (*arrowheads*)

CAA on the Boston criteria in the Table 3) [11]. Similar to the distribution of CAA pathology and CAA-related lobar ICHs, the distribution of CAA-related MBs appears to show a posterior cortical predominance (Figs. 1, 2 and 6) [18]. GRE sequences are the recommended method for MB detection due to the insensitivity of MB detection on CT and spin-echo sequences of MRI. Furthermore, considering the limitation of conventional T2* GRE sequences, which have underestimated MBs in 25 % of CAA patients, more sensitive sequences such as SWI and PRESTO sequences should be used to increase the detection rates of MBs (Fig. 1) [9]. It is notable that neuroimaging study has revealed lobar MBs in more than 20 % of patients with AD (Fig. 7), which may reflect advanced CAA in keeping with neuropathological findings [23].

Table 3 Classic and modified Boston criteria [11, 19]

	Classic Boston criteria	Modified Boston criteria
Definite CAA	Full post-mortem examination demonstrating: - Lobar, cortical or corticosubcortical haemorrhage - Severe CAA with vasculopathy - Absence of other diagnostic lesion	No modification
Probable CAA with supporting pathology	Clinical data and pathological tissue (evaluated) haematoma or cortical biopsy) demonstrating: - Lobar, cortical or corticosubcortical haemorrhage - Some degree of CAA in specimen - Absence of other diagnostic lesion	No modification
Probable CAA	Clinical data and MRI or CT demonstrating: - Multiple haemorrhages restricted to lobar, cortical or corticosubcortical regions (cerebellar haemorrhage allowed) - Age ≥55 - Absence of other cause of haemorrhage	Clinical data and MRI or CT demonstrating: - Multiple haemorrhages restricted to lobar, cortical or corticosubcortical regions (cerebellar haemorrhage allowed), or - Single lobar, cortical, or corticosubcortical haemorrhage and focal or disseminated superficial siderosis - Age ≥55 - Absence of other cause of haemorrhage or superficial siderosis
Possible CAA	Clinical data and MRI or CT demonstrating: - Single lobar, cortical or corticosubcortical haemorrhage - Age ≥55 - Absence of other cause of haemorrhage	Clinical data and MRI or CT demonstrating: - Single lobar, cortical or corticosubcortical haemorrhage, or - Focal or disseminated superficial siderosis - Age ≥55 - Absence of other cause of haemorrhage or superficial siderosis

Subarachnoid haemorrhage: a predictive finding of unfavourable outcomes?

Recently, CAA has been increasingly reported as a cause of SAHs in the elderly, especially those localised at the convexity of the brain (cSAH) [24, 25]. CAA-related cSAH may be due to direct extension of the cortical-subcortical haemorrhage into the subarachnoid or to primary SAH resulting from disruption of the leptomeningeal vessels by β-amyloid (Figs. 4 and 6) [8]. The clinical presentation of CAA-related cSAH is distinct because patients suffer from transient focal neurological deficits, including motor or sensory symptoms and seizures, rather than typical headaches [24, 25]. Such symptomatic cSAHs are mainly located within the central sulcus. Whether cSAH could be a warning sign of subsequent ICHs depends on the underlying disease. CAA-related cSAH often recurs, and a high rate of subsequent cerebrovascular disorders including infarctions and ICHs could contribute to unfavourable outcomes, including neurological disability and death in the elderly [25, 26].

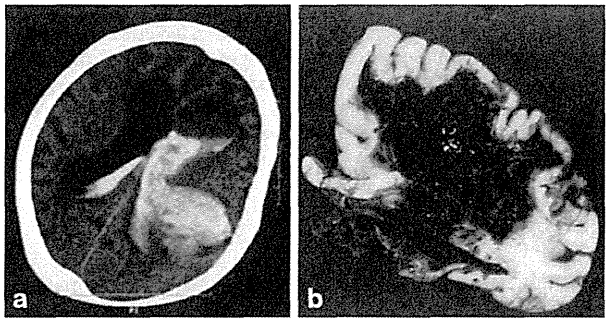

Fig. 3 Fetal CAA-related ICH with associated massive ventricular haemorrhage in a 92-year-old woman. A CT scan (**a**) revealed large left-sided parietal subcortical ICH extending into the left lateral ventricle, which caused hydrocephalic ventricular dilatation. A huge subcortical and intraventricular haematoma was identified on a macroscopic specimen at autopsy (**b**)

Unenhanced head CT has shown a slight, sometimes barely visible, sulcal hyperattenuation, most frequently depicted around the precentral gyrus [26]. Subsequent MRI scans confirmed the subarachnoid haemorrhage as a hyperintense area on FLAIR images (Fig. 6). In addition to this subarachnoid lesion, GRE sequences, especially SWI and PRESTO images, showed multiple lobar cortical-subcortical haemorrhagic lesions (macrohaemorrhages or MBs) (Fig. 6) [24, 25]. Considering the high prevalence of MBs and SS in CAA patients [24], these abnormal findings should be evaluated in the diagnosis of cSAH. It is also to be noted that CAA-related cSAH and SS can be present without other haemorrhagic lesions, including ICHs and MBs [19].

Superficial siderosis: a clinical entity distinct from the well-known classical SS

It is estimated that repeated cSAH leads to haemosiderin deposits in the subpial layers of the supratentorial brain [19].